Chapter 3 – Equilibrium, Flux Surface Integrity and Island Healing

This chapter discusses the NCSX equilibrium calculations, including the issue of flux surface integrity. The VMEC equilibrium code has been used for the routine generation of three-dimensional equilibria for stability and transport studies and has been incorporated in the optimizer for generating candidate NCSX configurations and assessing coil-set flexibility. The VMEC code is described in Section 3.1. Equilibrium calculations have used bootstrap-consistent current profiles, and the calculation of the bootstrap current is discussed in Section 3.2. Calculation of three-dimensional equilibria with islands and stochastic regions has been done with the PIES code, which is described in Section 3.3. Section 3.4 discusses the evaluation of flux surfaces for candidate configurations generated by the optimizer. Flux surfaces are destroyed by resonant fields, and Section 3.5 describes how the resonant fields in PIES may be calculated using quadratic-flux minimizing surfaces.

Once calculated, the resonant fields can be eliminated. Section 3.6 describes a method that has been used to make small modifications to the fixed-boundary NCSX configuration to remove residual magnetic islands. This procedure is adapted to free-boundary equilibria and Section 3.7 describes a procedure based on the PIES code to modify the coil design to remove resonant Fourier components generated by the discrete coils that cause flux surface breakup. This procedure is called island healing, and the coil set thus obtained is called the (M45h) healed coil set and is referred to throughout this document. Section 3.7 also includes results from multi-filament (as opposed to single filament) healed coil set calculations used to model the finite thickness of the coils, various vacuum configurations with the healed coils, and an equilibrium at β=4.6% comparing the healed coils to the unhealed coils.

The calculations described in sections 3.3 – 3.7 do not include neoclassical effects, which are expected to reduce island widths, and they do not include the effects of plasma flow, which can shield rational surfaces from resonant magnetic field components and prevent the formation of islands. The expected consequences of neoclassical effects are estimated in Section 3.8, and the effects of plasma flow are discussed in Section 3.9.

3.1 VMEC

The VMEC code[1] solves the three-dimensional equilibrium equations using a representation for the magnetic field that assumes nested flux surfaces. VMEC uses an inverse moments method, in which the geometric coordinates R and Z are expanded in Fourier series in a poloidal angle and toroidal angle (for non-axisymmetric configurations). The coefficients R_{mn}, Z_{mn} in this series expansion are functions of the normalized toroidal flux s, where s=0 is the magnetic axis (which can be a helical curve in three dimensions) and s=1 is the plasma boundary. Here, m is the poloidal and n is the toroidal Fourier mode number. The boundary Fourier coefficients $R_{mn}(s=1)$ and $Z_{mn}(s=1)$ can either be constant (corresponding to a "fixed-boundary" equilibrium calculation), or they may be self-consistently computed from the MHD force balance equation at the plasma-vacuum boundary (for a "free-boundary" calculation[2]).

Internally, VMEC computes an addition "renormalization" stream function, λ, which is used to optimize, dynamically and at every radial surface, the convergence rate in Fourier space

for the spectral sum $\Sigma(R_{mn}^2 + Z_{mn}^2)$. In the original VMEC, the radial mesh grid is staggered, with the $R_{mn}(s)$ and $Z_{mn}(s)$ coefficients defined on integral radial mesh points $s_j = (j-1)/(N_s-1)$, where N_s is the number of radial surfaces, and the lambda coefficients on half-integer mesh points interleaving the s_j mesh. This scheme has been proven to lead to excellent radial resolution as well as minimal mesh separation (at least for large aspect ratio plasmas and with limited angular resolution meshes).

Significant improvements have been made to the VMEC code in the context of the NCSX design effort. It has been re-differenced to improve the convergence both on finer angular and radial meshes and for equilibria with a wide range of rotational transform profiles. In VMEC, the inverse equations are cast as second order equations (in minor radius) for the Fourier components of R, Z, and λ. As noted above, λ has been previously differenced radially on a mesh centered between R, Z nodes, which greatly improved the radial resolution. This could be done to second order accuracy (in $h_s = 1/[N_s-1]$) since no radial derivatives of λ appear in its defining equation, $J^s = 0$ (here, J^s is the contravariant radial component of the current). Near the magnetic axis, however, a type of numerical interchange instability (mesh separation) has been observed as the angular resolution is refined. This behaviour has prevented the temporal convergence of 3D solutions with large numbers of poloidal (m) and toroidal (n) modes (typically, $m \sim 6$-8 was the practical limitation). It has also produced convergence problems for equilibria with low ι ($<<1$) where field lines must encircle the magnetic axis many times to define magnetic surfaces. The new differencing scheme computes the stream function on the same mesh as R and Z (although the output values of λ continue to be on the centered-grid for backwards compatibility), which leads to numerical stabilization of the origin interchange. To avoid first order errors (in h_s) near the plasma boundary resulting from the new representation of λ, the radial current J^s continues to be internally represented (in terms of λ) on the interlaced-grid. This maintains the good radial spatial resolution associated with the original half-grid representation for λ. As a result, computation of accurate, convergent solutions with substantially higher mode numbers is now possible using VMEC ($m < 20$). This corresponds to much finer spatial resolution and significantly improved force balance in the final equilibrium state. It also allows the calculation of equilibria with lower values of ι, which were difficult to obtain with the previous differencing scheme.

An additional improvement in the output from VMEC includes a recalculation (once the VMEC equilibrium has been obtained) of the magnetic force balance $\mathbf{F} \equiv \mathbf{J}\times\mathbf{B} - \nabla p = 0$. The radial ($\nabla s$) component of $\mathbf{F}$ is solved in terms of the non-vanishing contravariant components of B (B^u and B^v) and the metric elements determined by VMEC, as a magnetic differential equation for B_s. An angular collocation procedure (with grid points matched to the Nyquist spatial frequency of the modes) is used to avoid aliasing arising from nonlinear mode coupling of the Fourier harmonics of R and Z in the inverse representation of the equilibrium equation. The accurate determination of B_s, together with the higher angular resolution afforded by the larger limits on the allowable m,n spectra in VMEC, permits an accurate assessment for the parallel current (which contains angular derivatives of B_s) as a function of poloidal mode number, to be performed.

3.2 Bootstrap Current Profile

The current profiles for the NCSX design have been determined by a bootstrap current calculation using VMEC equilibria. Axisymmetric calculations using the bootstrap module in the jsolver code [3-5] have been used for this purpose. For perfect quasi-axisymmetry, the bootstrap current is identical to that in an equivalent tokamak, because the bootstrap current is determined by the Fourier components of |B| in Boozer coordinates. In practice, the quasi-axisymmetry condition is satisfied approximately, so to quantify the errors introduced by the residual non-quasi-axisymmetric ripple, fully three-dimensional Monte-Carlo-δf bootstrap calculations have been done for an earlier NCSX reference configuration, configuration C82, using the ORBIT code [6, 7]. These calculations have verified that the bootstrap current is given to a good approximation by the axisymmetric terms alone. The Monte-Carlo simulations for the non-axisymmetric case have been further benchmarked against calculations with the DKES (Drift Kinetic Equation Solver) code [8]. In calculating the bootstrap current with the JSOLVER code, the density profile has been taken to be $n(s) = n(0)(1-s^{2.3})^{0.1}$, where $n(0) = 0.54 \_ 10^{20}$ m^{-3}. The corresponding temperature profile for the full, 4% β, li383 case is $T(s) = T(0)(1-s^{2.3})^{1.9}$, where $T(0) = 2.14$ kev.

3.3 The PIES Code

Three-dimensional magnetic fields in general have magnetic islands and regions of stochastic field lines. The VMEC code uses a representation of the magnetic field that assumes nested flux surfaces, and thus cannot be used to examine magnetic islands. The PIES code is a three-dimensional equilibrium code that uses a general representation for the field, and is used for calculating islands and stochastic field line trajectories. There is an extensive set of publications on the algorithm, implementation, validation, convergence properties and applications of the PIES code. [9-13, 16-40]

The PIES code solves the MHD equilibrium equations using a Picard iteration scheme :

$$\nabla \times \mathbf{B}^{n+1} = \mathbf{J}(\mathbf{B}^{n}). \qquad (3\text{-}1)$$

The iterative steps involve solving the plasma current, **J**, given the magnetic field, **B**, and pressure gradient **∇**p :

$$\nabla p = \mathbf{J}^{(n+1)} \times \mathbf{B}^{n} \qquad (3\text{-}2)$$

$$\nabla \cdot \mathbf{J} = 0. \quad T\nabla \times \mathbf{B}^{(n+1)} \qquad (3\text{-}3)$$

with the constraint $\nabla \cdot \mathbf{B}^{n+1} = 0$, where $\mathbf{B}^{n}$ is the magnetic field at the start of the n^{th} iteration. This scheme is closely related to the Picard algorithm widely used to solve the axisymmetric Grad-Shafranov equation in the form $\Delta^* \psi_{n+1} = j_\phi(\psi_n)$. As with the Picard iteration scheme for the Grad-Shafranov equation, under-relaxation is used to extend the domain of convergence of the Picard iteration.

$$\mathbf{B}^{(n+1)} = \alpha\, \mathbf{B}^{n} + (1-\alpha)\, \mathbf{B}, \qquad (3\text{-}4)$$

where $0 < \alpha < 1$. An advantage of the Picard scheme is that it provides an accurate calculation of resonant pressure driven currents, which are believed to play an important role in determining island widths. At each iteration, the code solves for the current from the force balance equation. Writing

$$\mathbf{J} = \mu\mathbf{B} + \mathbf{J}_\perp, \ \mathbf{J}_\perp = \mathbf{B} \times \nabla p / B^2, \tag{3-5}$$

gives,

$$\mathbf{B} \cdot \nabla\mu = -\nabla \cdot \mathbf{J}_\perp. \tag{3-6}$$

Integration of this magnetic differential equation gives an accurate method for determining the currents. This follows the work of Gardner and Blackwell [41], who demonstrated the importance of using an accurate solution for the currents in stability studies, and it is now routine in Mercier and global stability studies of stellarators to recalculate the current from three-dimensional equilibrium solutions in this way. In implementing a numerical scheme for solving the magnetic differential equation, explicit upper bounds on the associated numerical errors were derived and are used to allow the specification of required tolerances in the code.[10]

As the PIES code iterates, the pressure and current are flattened in islands and stochastic regions. Several numerical diagnostics in the code allow the determination of the location of these regions. The PIES algorithm is described in detail in the references [9-13, 19].

The PIES code has been validated by testing of the individual components, by internal checks in the code that monitor the accuracy with which the equilibrium equations are satisfied, and by comparison with analytic solutions and with other codes. Analytic solutions against which the code has been compared have included : Soloveev equilibria[11]; large aspect ratio stellarator expansions[11]; helical force-free Bessel function equilibria with islands[19]; and the analytic solutions of White et al for saturated tearing modes with narrow islands. Comparison of PIES with other codes has included: comparison with axisymmetric j-solver[14]; equilibria for TFTR and DIII-D; comparison with Biot-Savart vacuum field solvers; comparison with marginal stability for tearing modes calculated by the linearized resistive time-dependent code of Hughes; and comparison with VMEC[16]. Reference [16] contains a careful comparison between the VMEC code and the PIES code solutions. The devices modeled were the ATF and TJ-II stellarators, for rotational-transform profiles where low order rational surfaces were absent. The flux surface shape, location of the magnetic axis and the value of iota as a function of flux surface were monitored as a function of β and radial resolution. An extrapolation in radial resolution was used to verify the quantitative agreement of the codes. The comparison with VMEC was continued in reference [18]. Here, the rotational transform as a function of radius was in excellent agreement between the two codes for the W7-X stellarator, at $< \beta > = 5\%$.

Many stellarators, for example ATF, TJ-II, W7-AS, W7-X and LHD have been modeled by the PIES code [11,16,18,20]. Present day experiments have not reached the predicted equilibrium beta limit, and no experimental study of this issue has therefore been possible.

In the context of the NCSX design effort, several modifications have been made to the PIES code that have increased its speed by about an order of magnitude, allowing routine

application of the code to evaluate flux surfaces in candidate NCSX configurations. The speed of the code was improved by modifications to use an improved method for PIES initialization with a VMEC solution, converting to a spline representation of the magnetic field for field line following, and to store matrix inverses. Compared with VMEC, the PIES code has a more time-consuming algorithm, which is needed for a general representation for the magnetic field. Time is saved by initializing PIES with a converged VMEC solution. For this purpose, the under-relaxation scheme in PIES has been modified to provided an improved coupling to the VMEC solution. This involves blending with the VMEC field in the first PIES iteration. The previous under-relaxation scheme blended the current rather than the fields. The under-relaxation was skipped in the first PIES iteration, allowing a large step from the VMEC field, but slowing the ultimate convergence. The PIES code follows magnetic field lines as a preliminary step to solving the magnetic differential equation determining the Pfirsch-Schlueter current. In each iteration of the PIES code, a discretized Ampere's law is solved by the inversion of a block-tridiagonal matrix. The elements of the blocks are determined by metric elements of a ``background coordinate system'' that does not change from one iteration to the next, allowing time to be saved by storing the inverses of the blocks. For high resolution calculations, this changes the scaling of the code's execution time from m^3n^3k to a much more favorable m^2n^2k where m and n are the number of the poloidal and toroidal modes retained, and k is the number of radial grid surfaces.

3.4 Flux Surface Integrity

Three-dimensional magnetic fields in general have magnetic islands and stochastic field lines. The goal is to minimize the size of these regions in NCSX to obtain good flux surfaces across at least 90% of the cross-section. As a first step, a fixed boundary reference configuration with relatively good flux surfaces was identified, and this configuration is referred to as LI383. The intrinsic flux surface properties of configuration LI383 relative to that of other configurations are discussed in this section. Section 3.6 will discuss adjustments of the LI383 boundary to remove residual islands. Section 3.7 will discuss the design of coils that preserve flux surfaces by suppressing magnetic islands – a procedure called coil healing.

The configuration optimizer used to generate candidate configurations for the NCSX design study did not include a measure of flux surface integrity. Flux surface calculations for the various candidate configurations have found significant differences in the extent of islands and stochastic regions. The earlier reference configuration, C82, was found to have a large region of stochastic field lines at beta values of interest. This was typical of several types of configurations that were studied. In contrast, the flux surfaces of the NCSX reference design configuration LI383 and similar configurations were nearly adequate even before the application of any flux surface optimization.

In regions where $d\iota/ds > 0$, perturbed bootstrap current effects are predicted to lead to substantially decreased magnetic island widths in configurations of the type studied here.[42] This is the inverse of the neoclassical tearing mode that has been observed in tokamak experiments. This neoclassical effect is presently being incorporated into PIES, but is not included in the calculations reported here. The calculations are therefore conservative in that the calculated island widths are likely to be larger than would be observed in an experiment operated

in a collisionless regime. Section 3.8 gives an estimate of the neoclassical effect on the island widths.

The PIES calculations discussed in this section are all fixed boundary, and used 143 Fourier modes, $0 \le m \le 11$, $-6 \le n \le 6$, and 60 radial zones.

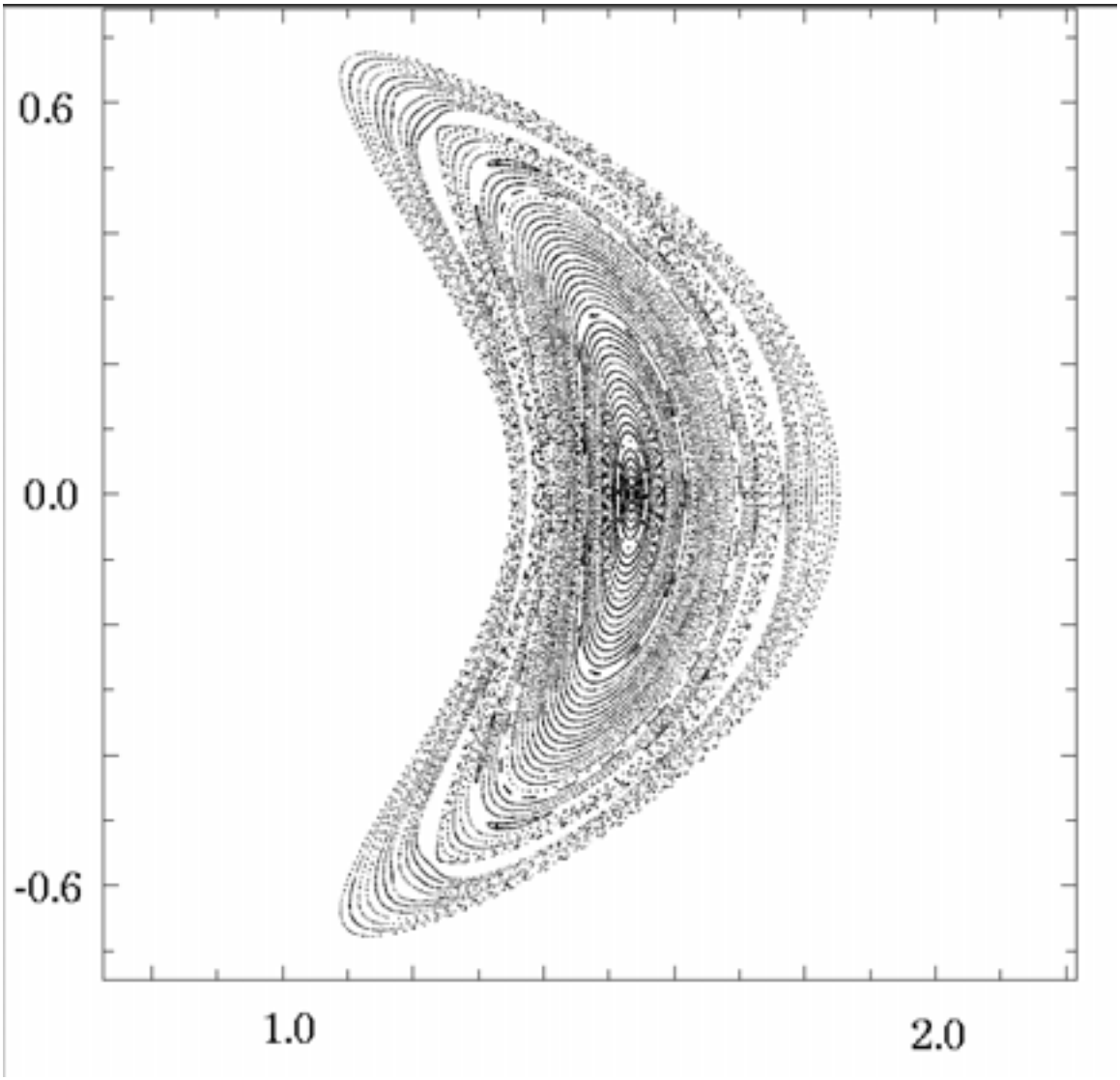

Figure 3-1. Poincare plot for configuration C82 at full current, $\beta = 0$

Figure 3-1 shows a Poincare plot of a fixed-boundary PIES equilibrium for configuration C82 at full current, $\beta = 0$. Magnetic islands occupy about 10% of the cross-section. The islands are more readily visible if the Poincare plot uses a polar (ρ, θ) coordinate system, as in Figure 3-2. Here, the coordinate ρ is taken to be constant on VMEC flux surfaces, and to measure the distance of the VMEC flux surface from the magnetic axis along the $\theta = 0$, $\phi = 0$ line. The angular coordinate θ is identical to the VMEC angular coordinate. When plotted in these coordinates, the Poincare plot gives straight lines when the VMEC and PIES solutions coincide.

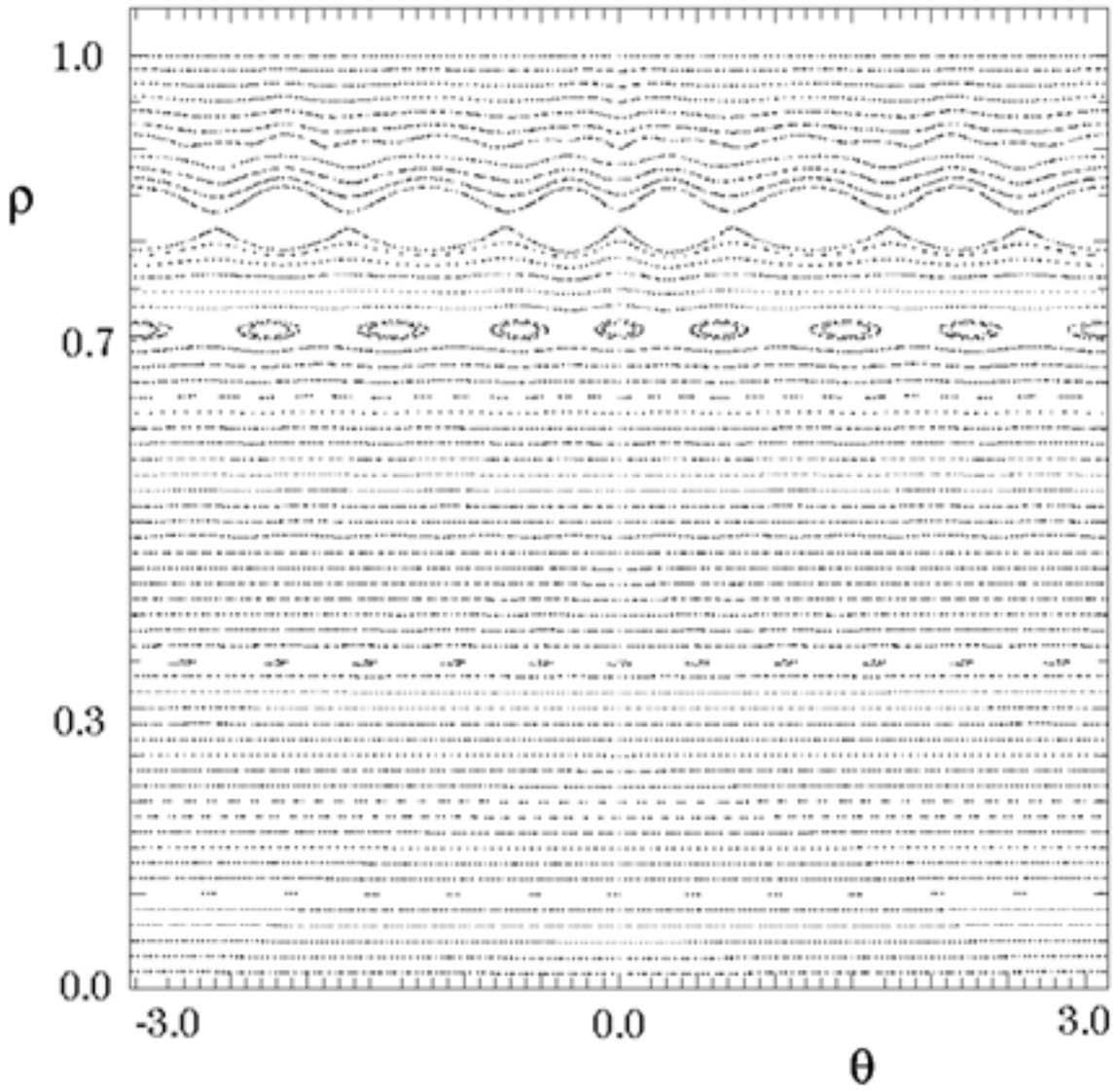

Figure. 3-2. Poincare plot for configuration C82 in VMEC coordinates, full current, β = 0

When β is raised to 3%, the PIES calculations find that a substantial fraction of the flux surfaces are lost (Figure 3-3). The equilibrium solution shown is not fully converged. The

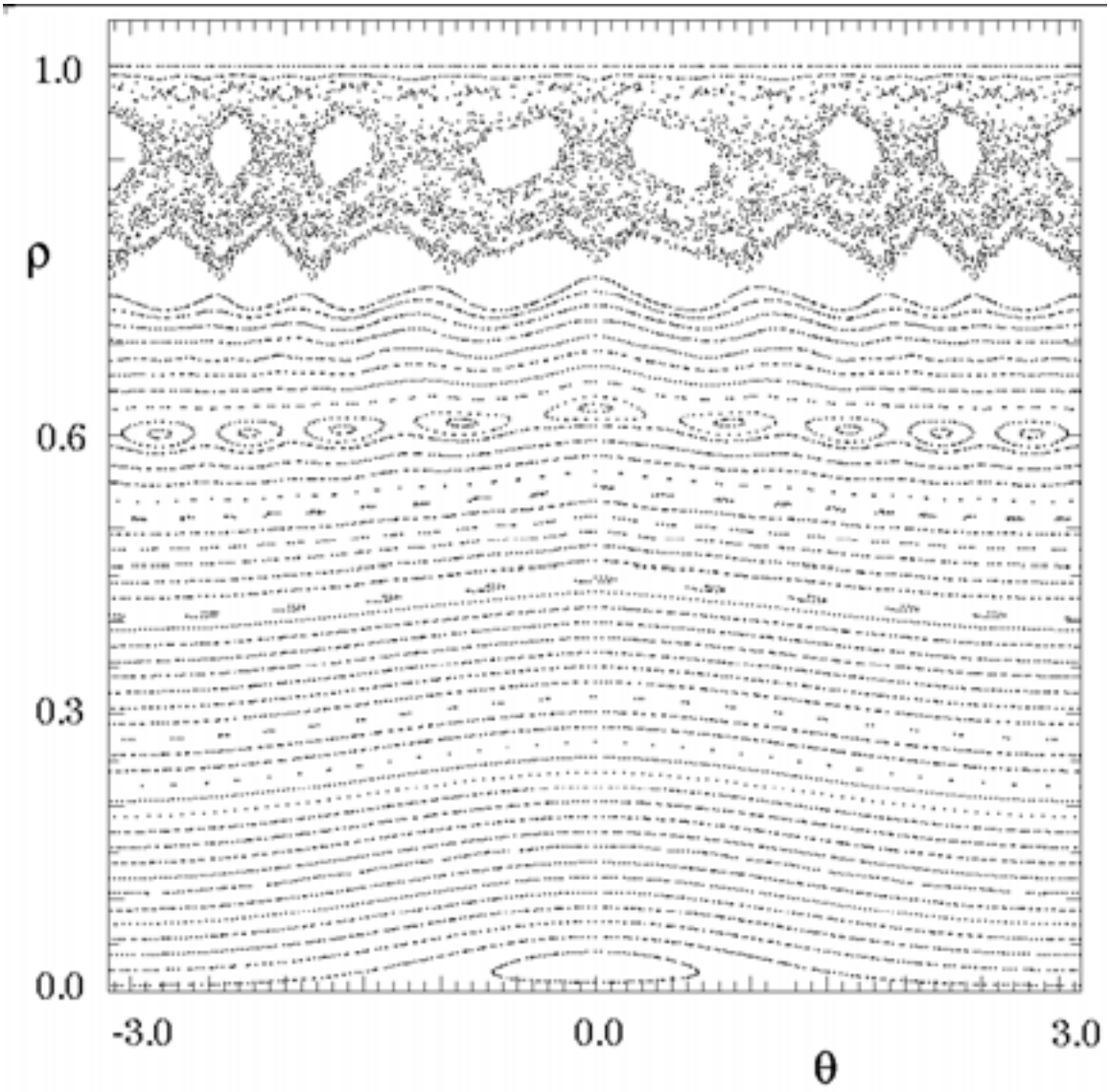

Figure 3-3. Poincare plot for earlier configuration, C82, at full current, β = 3%

outer surfaces continue to deteriorate as the calculation progresses, so that further computation is of limited interest. From these plots we conclude that flux surface integrity is a problem for configuration C82 in the absence of stabilizing neoclassical effects.

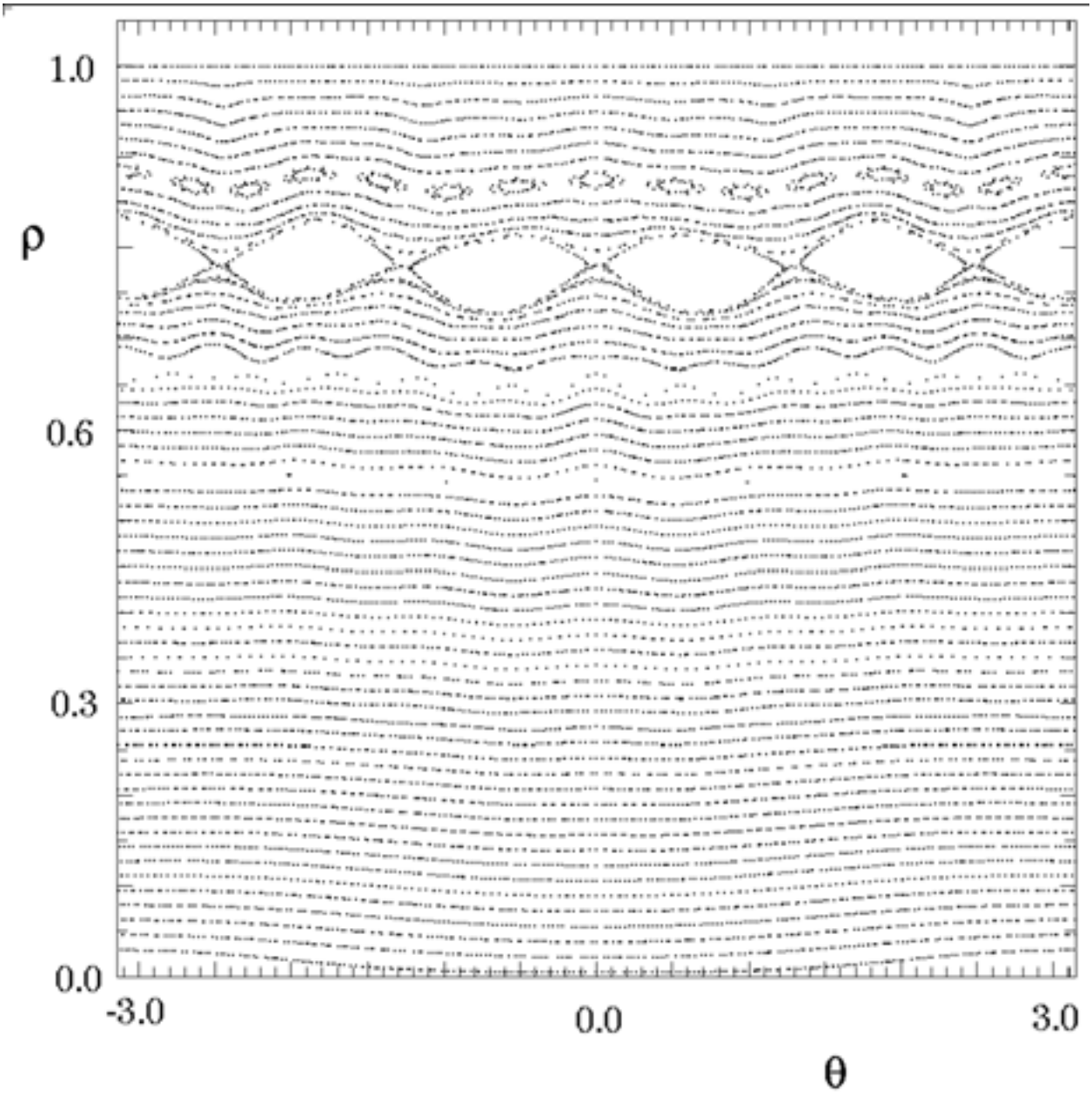

Figure 3-4. Poincare plot for configuration LI383 at full current, β = 4.2%

Figure 3-4 shows the result of a PIES calculation for configuration LI383 as originally generated by the optimizer at full current, β = 4.2%. The flux surfaces are greatly improved relative to those of configuration C82. The total island width is about 15%, and is dominated by a single island chain at ι =0.6 having poloidal and toroidal mode numbers m=5 and n=3.

The fact that the flux surface loss in the original configuration LI383 is dominated by a single island chain suggests that the flux surfaces can be further improved by adjusting the

amplitude of the corresponding resonant Fourier mode in the specification of the boundary shape. This has been demonstrated, and is discussed in the following sections.

3.5 Resonant Fields, Islands and Quadratic-Flux Minimizing Surfaces

Magnetic islands are caused by resonant radial magnetic fields where the rotational transform is a rational value. The continuous one-dimensional family of periodic orbits that form a rational rotational transform flux surface in the absence of resonant fields will be reduced to a finite set of periodic orbits by the resonant field, and an island chain will form. The periodic orbits surviving perturbation will typically be the stable and unstable periodic orbits, which correspond to the O and X points on Poincare plots of the magnetic field. In the small island approximation, where the shear, ι', is assumed constant across the island, the width of the island is given [44] as $w \propto (|B_{nm}|/\iota' m)^{1/2}$, where $B_{nm} = (\mathbf{B} \cdot \nabla s / \mathbf{B} \cdot \nabla \phi)_{nm}$ is the resonant Fourier component of the radial field at the $\iota = n/m$ rational surface, s is the radial coordinate, and the prime represents derivative with respect to s. The phase of the island chain is determined by the sign of B_{nm} and the sign of the shear.

A method for calculating resonant fields at rational surfaces has been incorporated into PIES. This method is based on the construction of quadratic-flux-minimizing surfaces. The construction of these surfaces has been presented in [Hudson & Dewar, Physics of Plasmas 6(5):1532,1999.]. The surfaces are defined as extremizing surfaces of the square of the action gradient functional which is defined

$$\_ = \_ \iint [\_S/\_\_]^2 \; d\_d\_, \tag{3-7}$$

where the action integral is

$$S = \oint \mathbf{A}.\mathbf{dl}, \tag{3-8}$$

and **A** is the magnetic vector potential and **dl** is a line segment. For the purposes the present discussion, quadratic –flux minimizing surfaces pass directly through the corresponding island chains, and may be considered as rational flux surfaces of an underlying integrable magnetic field.

The construction of the quadratic-flux-minimizing surfaces, in essence, provides an optimal magnetic coordinate system, or equivalently an optimal nearby integrable magnetic field, and in these coordinates resonant perturbation harmonics are easily identified. The method is computationally efficient as the quadratic-flux-minimizing surfaces defining the coordinate system may be constructed exactly and only where required -- at the rational rotational-transform surfaces where islands develop. The amplitude of each selected resonant field harmonic is calculated by Fourier decomposing the magnetic field normal to the quadratic-flux-minimizing surface. Furthermore, and importantly, the Fourier decomposition is performed using an angle coordinate that corresponds to a straight field line coordinate of the underlying integrable field on that surface.

The rotational-transform profile determines which islands will be present in a given configuration, and islands associated with low-order rationals are typically the largest; however; where the shear is small higher-order islands can easily overlap and result in chaotic field lines and loss of confinement. For the case of LI383, the islands selected for suppression are typically those corresponding to _=0.5,0.6, though higher order islands are also considered at times. Generally the lowest order resonances present will produce the largest magnetic islands. A convenient method of selecting the lowest order rationals is guided by the Farey Tree construction [45].

3.6 Healing of Fixed-Boundary Flux Surfaces

In this section we consider manipulation of the width and phase of magnetic islands in finite β stellarator equilibria as calculated by PIES by making small variations to the boundary [Hudson, Monticello & Reiman, Physics of Plasmas, 8(7):3377 2001.]. Magnetic islands are controlled by adjusting the resonant fields at the rational surfaces.

A set of islands that we wish to control is selected. In the case of LI383, clearly the (n,m)=(3,5) island is dominant. The corresponding set of resonant fields that need to be controlled is represented by

$$\mathbf{B} = (B_{n1,m1}, B_{n2,m2}, \ldots)^T. \qquad (3\text{-}9)$$

We expect that an (n,m) island width will be strongly affected by an (n,m) resonant deformation of the plasma boundary in magnetic coordinates and perhaps through coupling to neighboring modes, so a set of independent boundary variation parameters is constructed as follows. We consider the minor radius

$$r = \sum r_{nm} \cos(m\theta - nN\phi) \qquad (3\text{-}10)$$

of the plasma boundary to be a Fourier series in the cylindrical toroidal angle and the poloidal angle used in VMEC to construct the input R and Z harmonics. The conversion to cylindrical space is given as $R = r\cos\theta$, $Z = r\sin\theta$. For a change $r \rightarrow r + \delta r_{nm} \cos(m\theta - nN\phi)$, the input Fourier harmonics for the VMEC code change according to

$$\begin{aligned} R_{m-1,n} &\rightarrow R_{m-1,n} + \delta r_{nm}/2,\ R_{m+1,n} \rightarrow R_{m+1,n} + \delta r_{nm}/2, \\ Z_{m-1,n} &\rightarrow R_{m-1,n} - \delta r_{nm}/2,\ Z_{m+1,n} \rightarrow R_{m+1,n} + \delta r_{nm}/2. \end{aligned} \qquad (3\text{-}11)$$

In principle we may change infinitely many boundary harmonics r_{nm}, but a small set is chosen to match the islands targeted and this becomes the vector of independent parameters

$$\mathbf{r} = (r_{n1m1}, r_{n2m2}, \ldots)^T. \qquad (3\text{-}12)$$

Now the problem is amenable to standard treatments where the functional dependence of **B** on **r** is represented

$$\mathbf{B}(\mathbf{r}_0 + \delta\mathbf{r}) = \mathbf{B}(\mathbf{r}_0) + \mathbf{C} \cdot \delta\mathbf{r} + \ldots ,$$

(3-13)

where $\mathbf{r}_0 = 0$ is the initial boundary shape and $\delta\mathbf{r}$ is a small boundary variation. The coupling matrix **C** represents derivative information and will in general be an M _N matrix, where M is the number of resonant fields, and N is the number of independent boundary variations. The *j*th column of the coupling matrix is determined through a VMEC/PIES run by making a small change $\delta r_{nj,mj}$ and taking the difference in the resonant fields from the original equilibrium, divided by the change. Hence, N+1 VMEC/PIES runs are required to determine the coupling matrix (each PIES run is initialized with a VMEC equilibrium).

The coupling matrix is inverted using the singular value representation [46], $\mathbf{C} = \mathbf{U}\mathbf{w}\mathbf{V}^T$, where U and V are ortho-normal and **w** is the diagonal matrix of singular values. If there are more variables than equations more than one solution may exist and the nullspace is spanned by the columns of U corresponding to zero singular values, of which there will be at least N-M. Islands are removed if $\mathbf{B} = 0$, so by choosing a correction to the boundary $\delta\mathbf{r}$ according to

$$\delta\mathbf{r}_{i+1} = - \mathbf{V}\mathbf{w}^{-1}\,\mathbf{U}^T\,\mathbf{B}_i, \tag{3-14}$$

where as in standard singular value decomposition techniques the zero, and if desired the small, eigenvalues are ignored in the inversion of **w**, and $\mathbf{B}_i$ is the vector of resonant fields at the ith iteration. In practice, several iterations will be required to achieve a desired accuracy.

This technique was applied to configuration LI383. A Poincare plot Figure 3-5 of the PIES field after 32 iterations shows island chains and the $\iota = 3/5$ island is significant. In this figure and the next, the Poincare section is the $\phi = 0$ plane and 50 field lines are followed starting along the $\theta = 0$ line. In addition, field lines at the X points of several low order island chains are followed and the quadratic-flux minimizing surface and an estimated separatrix has been plotted over one period of each island chain. The separatrix of the island chains has been calculated using the resonant radial field and the shear at the rational surface of the VMEC equilibrium. PIES has not yet converged for this case, but the information about the island width is still useful for construction of the coupling matrix. To iterate each PIES run to convergence requires excessive cpu time.

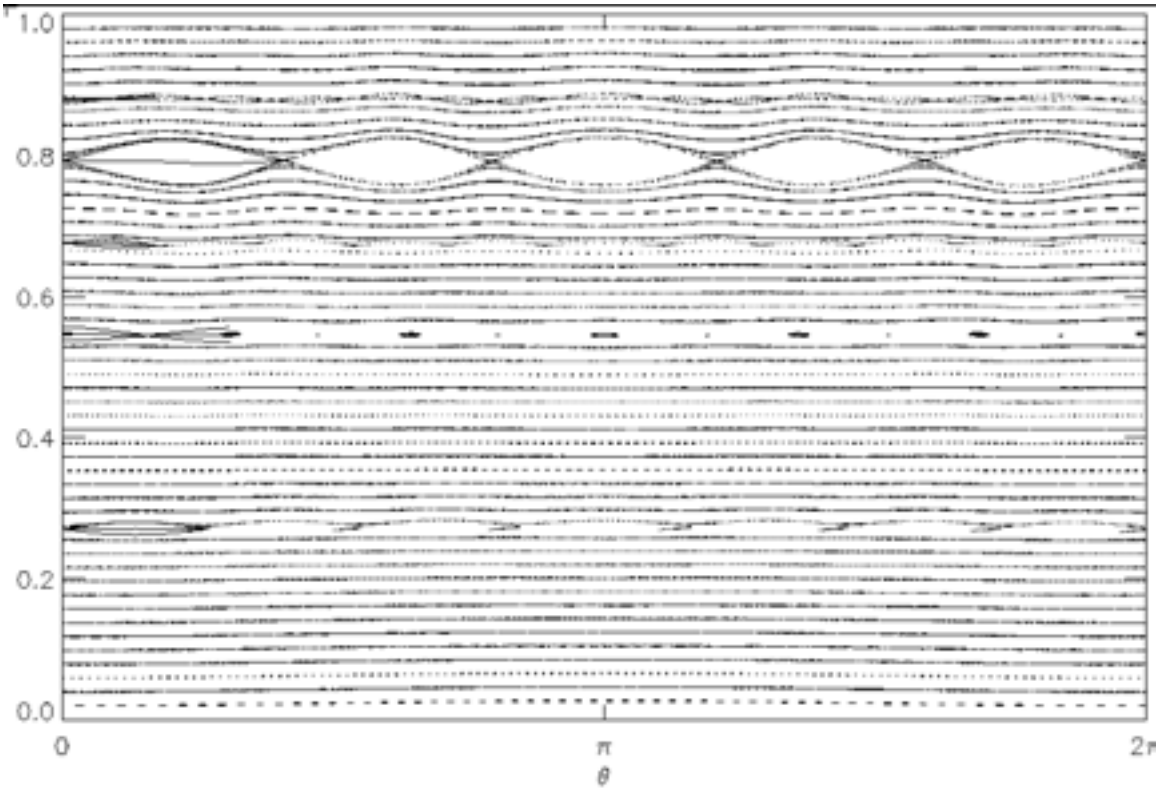

Figure 3-5. Poincare plot of initial LI383 configuration after 32 PIES iterations

In this application of the island reducing technique, the (3,5),(6,10),(3,6) and (6,12) resonances are targeted, and the (3,9),(3,8),(3,7),(3,6),(3,5) and (3,4) boundary harmonics are varied. The (6,10) resonance produces an island at the same rational surface as the (3,5), namely at $\iota = 3/5$, and may be considered as the second harmonic of the (3,5) resonance. If the (6,10) resonant field is not targeted, this may cause an island of distinct topology from the (3,5). The (3,6) and (3,12) resonances are included to ensure elimination of the (3,5) island does not cause a (3,6) island to grow. The (3,7) resonance is also present in the configuration, but this has not been included. For this set of resonant fields and independent boundary variation parameters, the coupling matrix is shown.

$$\begin{bmatrix} \delta B_{3,5} \\ \delta B_{6,10} \\ \delta B_{3,6} \\ \delta B_{6,12} \end{bmatrix} = \begin{bmatrix} -0.15603, & 0.94645, & -0.73397, & -1.13506, & -0.17282 & -0.30578 \\ 0.12627, & 0.17790, & 0.02146 & 0.19875, & -0.07025, & 0.01394 \\ -0.05487, & -0.22773, & -0.50056, & 0.24140, & -0.30079, & 0.01531 \\ -0.00874, & 0.03067, & -0.00351, & 0.00827, & -0.00327, & -0.00083 \end{bmatrix} \begin{bmatrix} \delta_{3,9} \\ \delta_{3,8} \\ \delta_{3,7} \\ \delta_{3,6} \\ \delta_{3,5} \\ \delta_{3,4} \end{bmatrix}$$

On performing the Newton iterations, the following reduction in resonant fields is observed.

iteration	$\lvert B_{3,5}\rvert$	$\lvert B_{6,10}\rvert$	$\lvert B_{3,6}\rvert$	$\lvert B_{6,12}\rvert$
0	1.8×10^{-3}	1.6×10^{-4}	1.3×10^{-4}	1.4×10^{-5}
1	1.3×10^{-4}	3.4×10^{-5}	1.0×10^{-4}	2.4×10^{-6}
2	6.7×10^{-5}	3.4×10^{-5}	5.1×10^{-5}	1.9×10^{-6}
3	2.4×10^{-5}	6.7×10^{-5}	4.0×1^{-16}	5.4×10^{-7}

Table 3-1

The Newton iterations are terminated after four steps as this provides sufficient reduction of the islands as seen in Figure 3-6. In a true Newton iteration procedure, the coupling matrix would be re-calculated at every iteration. In this application such a procedure is too slow and the coupling matrix is not changed; nevertheless, the convergence is satisfactory. The total change in the boundary variation parameters is

$$\delta \mathbf{r} = (-0.00184,-0.00026,0.00056,0.00300,0.00012,0.00064)^T. \qquad (3\text{-}15)$$

These variations are several millimeters in magnitude and generally have little impact on stability and other physics. However, the case shown does destabilize the ballooning modes on some surfaces. This would be expected to relax the pressure gradient slightly on those surfaces. This is not surprising considering that the LI383 configuration has been optimized to provide marginal ballooning stability at full pressure.

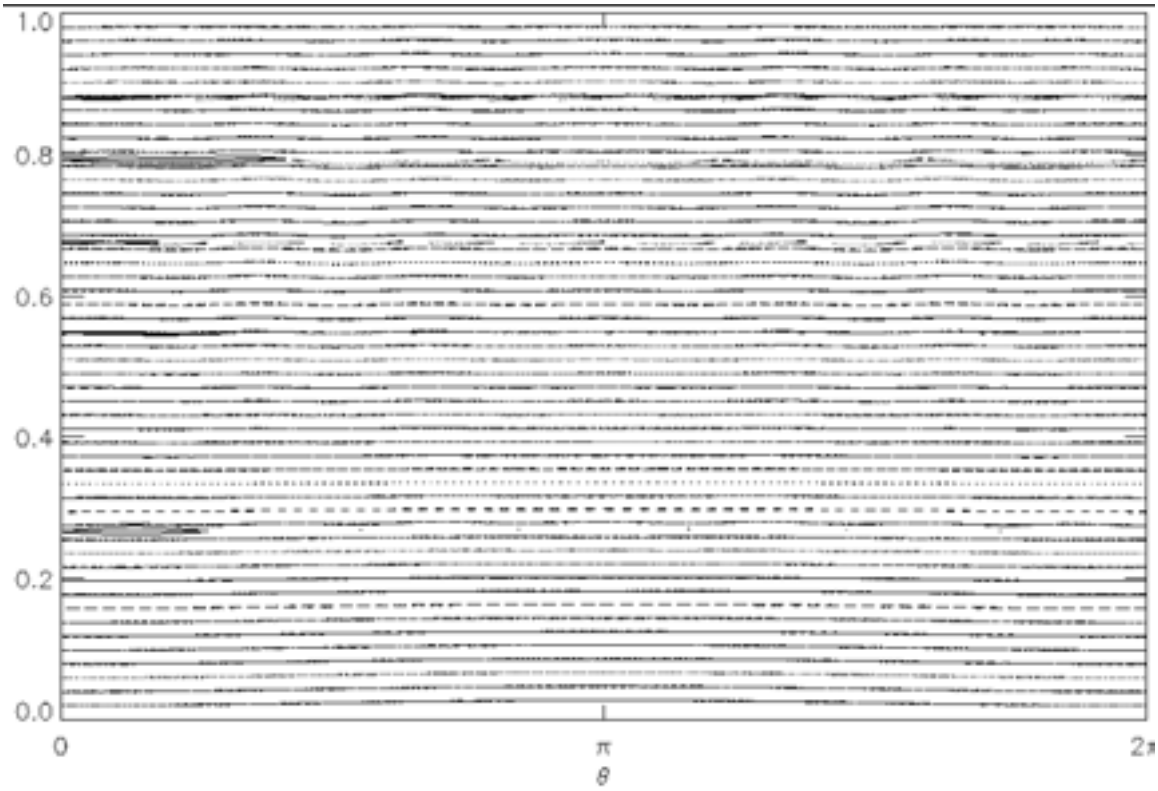

Figure 3-6. Poincare plot of full-beta island-reduced LI383 configuration

The healed configuration has converged after 32 iterations, as has been confirmed by an extended PIES run for hundreds of iterations. If the equilibrium has no islands, or if the width of the islands is less than the radial grid used in PIES, then PIES and VMEC will agree and PIES will rapidly converge.

3.7a Healing of Free-Boundary Flux Surfaces `Coil-healing_ : Algorithm.

The previous two sections have discussed the design of the fixed boundary configuration to obtain good flux surfaces in equilibria where the shape of the boundary is specified. In the coil design process, a discrete set of coils is produced which targets the desired boundary shape, and the coils are further modified using the merged optimizer to allow for the simultaneous targeting of engineering and physics objectives in the coil design. The result is a plasma that is stable to ideal modes and a coil-design that is buildable; however, flux surface quality is not guaranteed by this process, and islands reappear in the free-boundary equilbria.

This section discusses the modification of the coils to heal the flux surfaces while preserving various engineering and physics measures, of the free-boundary equilbrium. The method is based on the free-boundary version of the PIES code. Island suppression is achieved by adding to the standard PIES algorithm a procedure that alters the coil geometry *at each iteration* so that selected resonant components of the coil magnetic field cancel the resonant components of the plasma magnetic field -- thus eliminating islands. The changes in coil geometry are constrained to preserve both engineering constraints and ideal kink stability. As the iterations continue, the coil geometry and the plasma simultaneously converge to an island-free coil-plasma equilibrium.

An early attempt [Hudson, Reiman, Strickler et al. to appear Plasma Physics and Controlled Fusion. *"Free-boundary full-pressure island healing in a stellarator : coil-healing."*.] at healing free-boundary PIES equilibria by variation of the coil-geometry calculated the resonant fields after a fixed number, N, of PIES iterations, in which the coil geometry was unchanged. The resonant fields were expressed as a function of coil geometry, and a method essentially identical to the fixed boundary healing method was used to vary the coil geometry to reduce the resonant fields after N iterations. This method had some success in healing coil sets, however; the PIES calculations were typically not converged after the fixed number N iterations and there was no guarantee that the configuration would remain healed (this is in contrast to the fixed boundary healing method, where PIES was initialized by the VMEC equilibrium for each trial boundary, which was not the case here). Experience from this work led to the method presently used to heal free-boundary surfaces – termed dynamical-healing – which alters the coil geometry at each PIES iteration and is now described.

The dynamical-healing procedure amounts to a free-boundary coil-physics optimizer that preserves good flux surfaces, satisfies engineering constraints and includes measures of physics stability. It is this procedure which leads to healed coil sets, and this procedure is also called coil-healing or island healing.

The dynamic healing procedure is obtained by including in the basic PIES the module COILOPT and STELLOPT which are used to alter the coil geometry and evaluate physics measures. Solving the equilibrium equation and the adjustment of a coil design to eliminate selected magnetic islands proceeds with initialization given

$$\mathbf{B} = \mathbf{B}_P^n + \mathbf{B}_C(\xi)^n. \qquad (3\text{-}16)$$

The total magnetic field is the sum of the magnetic field produced by the plasma, $\mathbf{B}_P$, and the magnetic field produced by the confining coils, $\mathbf{B}_C$, which is a function of a set of Fourier harmonics, $\boldsymbol{\xi}$, which describe the coil geometry, at the *n*th iteration. The initial plasma state is provided by the VMEC code, which imposes the artificial constraint that the plasma is consistent with nested flux-surfaces. The constraint of nested flux-surfaces forces stellarator equilibria to contain singular currents at the rational surfaces. The method presented in this section can be considered as removing this constraint and allowing the VMEC initialization to relax into an equilibrium, potentially with broken flux-surfaces (islands), while making adjustments to the coil set to remove selected islands as they develop. The initial coil-geometry is provided by the COILOPT code.

As described before, the standard PIES algorithm will calculate the plasma current from the field, and then the plasma field from the current. The additional steps in the implementation of the coil-healing are as follows. The total magnetic field, **B,** after one PIES iteration is written

$$\underline{\mathbf{B}} = \mathbf{B}_P^{(n+1)} + \mathbf{B}_C(\xi)^n. \qquad (3\text{-}17)$$

We may consider $\underline{\mathbf{B}}$ as a small perturbation to a nearby integrable field and that magnetic islands are caused by fields normal to, and resonant with, rational-rotational-transform flux-surfaces of the nearby integrable field. A set of resonances that are to be suppressed is selected, for each

resonance a quadratic-flux-minimizing surfaces is constructed, and the set of resonant fields thus calculated is denoted $\{\underline{B}_i : i=1,N\}$.

The COILOPT code provides a convenient Fourier representation of the coil geometry and a set of coil harmonics $\{\xi_j : j=1,M\}$ appropriate for the resonances selected are systematically varied to set $\underline{B}_i=0$ using a Newton method. The coupling matrix, $\nabla\mathbf{B}_{Cij}^n$, is defined as the partial derivatives of the selected resonant harmonics of the coil magnetic field normal to the quadratic-flux-minimizing surface (held constant during each PIES-healing iteration) with respect to the chosen coil harmonics and is calculated using finite-differences. A multi-dimensional Newton method is applied to find the coil changes $\delta\xi_j$ that set $\underline{B}_i=0$.

$$\underline{B}_i=\nabla\mathbf{B}_{Cij}^n\bullet\delta\xi_j^n. \qquad (3\text{-}18)$$

This equation is solved for the $\delta\xi_j$ in a few iterations by inverting the N×M matrix $\nabla\mathbf{B}_{Cij}^n$ using singular-value decomposition and the new coil set is obtained

$$\xi_j^{(n+1)}=\xi_i^n+\delta\xi_j^n, \qquad (3\text{-}19)$$

such that the resonant component of the combined plasma-coil field is eliminated. As the iterations proceed, the coil geometry and the plasma simultaneously converge to coil geometry-plasma solution with good-flux-surfaces.

The algorithm as presented is insufficient for practical purposes as no consideration has been given to various engineering constraints. To be `build-able', the minimum coil-curvature and coil-coil separation, for example, of the coils must exceed certain limits. Such constraints are included in the COILOPT code and the initialization coil set, described by $\boldsymbol{\xi}^0$, is satisfactory from an engineering perspective. The healing algorithm is modified to preserve the minimum curvature and coil-coil separation by adding to the set of resonant fields to be eliminated the (appropriately weighted) differences in minimum curvature and coil-separation of the nth coil set, described by $\boldsymbol{\xi}^n$, from the initial coil set. This constrains the island-eliminating coil variations to lie in the nullspace of these measures of engineering acceptability.

In a similar manner, the algorithm is extended to preserve kink stability. The VMEC initialization is stable with respect to kink modes. By calculating kink stability using the TERPSICHORE and VMEC codes which are executed via the STELLOPT routine, the coil changes are constrained to preserve kink stability.

3.7b Application of Coil-Healing to M45 coils _Healed Coils M45h.

Considering now the M45 coil set and selecting the (n,m)=(3,6),(3,5) islands to be suppressed, subject to the constraint that the minimum coil curvatures, the coil-coil separation and the kink stability be preserved (9 constraints), and allowing some m=3,4,5,6,7,8 modular coil harmonics to vary (36 independent variables), a healed coil-plasma state is achieved. The engineering measures are preserved and the plasma is stable with respect to kink modes. The plasma retains quasi-axis symmetry. Several hundred iterations are required to approach convergence in both the plasma field and the coil geometry. To confirm that the coil set is healed several hundred additional standard PIES iterations are performed with the coil set unchanged. The coil set obtained is called the healed M45 coil set and is renamed M45h.

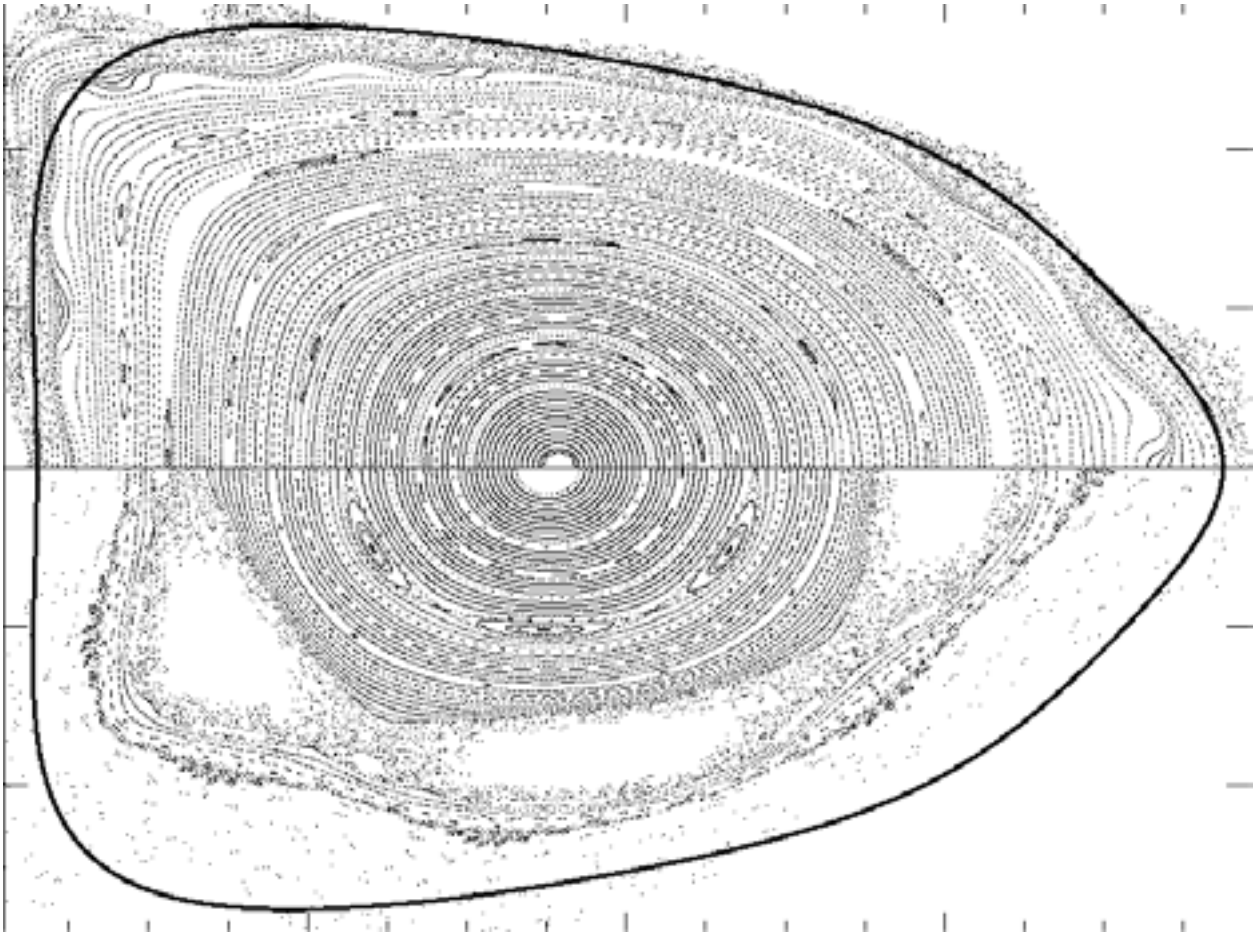

Figure 3-7. Poincare plots before (lower) and after (upper) free-boundary healing of flux surfaces from M45 coils. β = 4.1%. The first wall boundary is shown as the solid line.

A Poincare plot of the final field is shown on an up-down symmetric toroidal cross-section in the upper half Figure 3-7. In this, and the similar plots to follow, the boundary of the first wall / plasma facing component is shown as a thick solid line. The island content in the healed configuration is negligible, though there is some resonant m=18 deformation near the zero shear location (indicating that additional *near*-resonant modes may need suppressing, or that the

maximum _ needs to be constrained to avoid the resonance) and some high order (m=10,11,12, and 14) island chains (which are considered sufficiently small). For comparison, a Poincare plot of the unhealed configuration is shown after 180 standard PIES iterations in the lower half of the figure. For the un-healed case there is a large m=5 island, the edge has become chaotic, and the configuration deteriorates into large regions of chaos as the iterations continue.

A broad selection of coil harmonics was varied as the coil harmonics are not decomposed in a magnetic angle and thus cannot be expected to couple directly with the resonant field harmonics of the plasma. Also, by doing so there is extra freedom which is utilized by the singular-value decomposition method to find a solution with minimal coil change. The coil harmonics varied actually describe the toroidal variation of the modular coils on a topologically toroidal winding surface. The winding surface itself is described using a Fourier representation, but the winding surface is not altered in this procedure. The calculation shown used 63 radial surfaces, 12 poloidal and 6 toroidal modes. Similar results have been obtained using up to 93 radial surfaces and 20 poloidal modes.

The maximum coil alteration is about 2cm, which comfortably exceeds manufacturing tolerances, but is not so large that `healing' significantly impacts other design concerns, such as diagnostic access. A plot of the original coils and the healed coils is shown in VMEC toroidal coordinates is shown below in Fig 3-8. From this figure we can see that the healed coils, from an engineering perspective, are essentially the same as the original coils; in particular, the coil-coil separation and minimum coil bend radius are the same for the M45h coils and the original M45 coils.

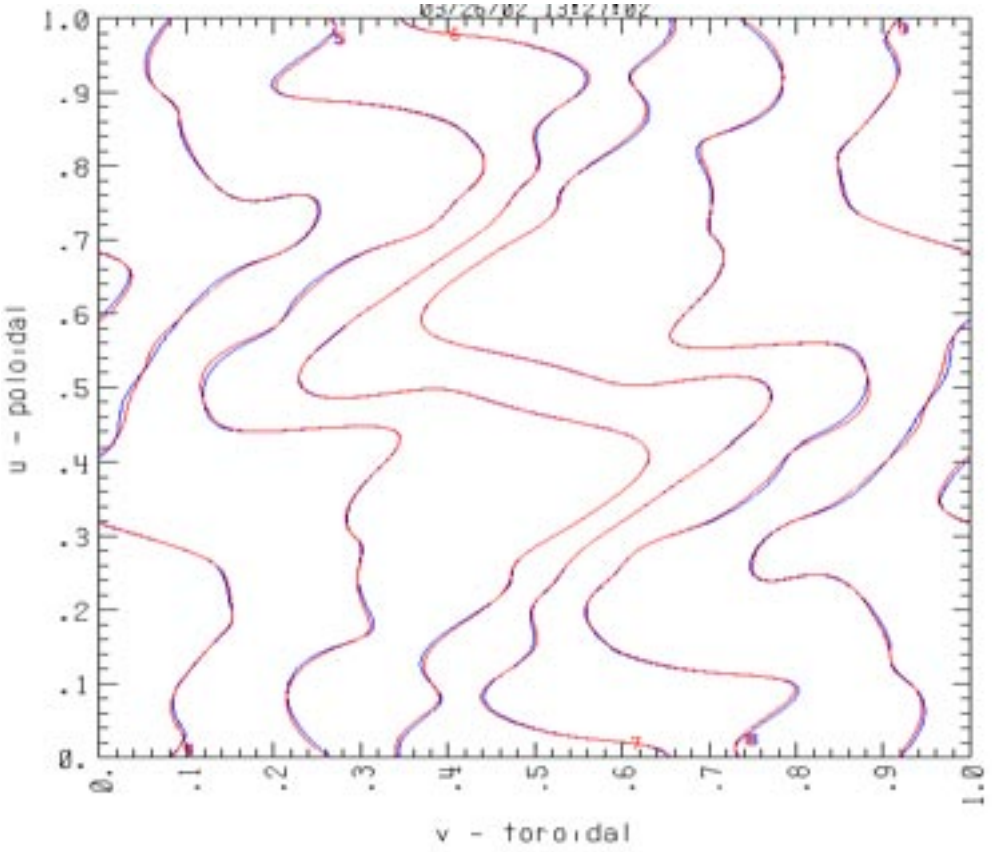

Figure 3-8. Original M45 coils and healed M45h coils in u-v space.

3.7.1 Finite Thickness Healed Coil Set

The analysis of coil sets thus far has used single filament coil representations. The single filament model simply positions a filament at the geometrical center of each coil along the winding path. As the difference between the healed and unhealed coils is about 2cm, it is required to confirm that the finite thickness of the coils to be built will not adversely affect the quality of the flux surfaces. A finite model coil configuration, based on the healed coil set, is obtained as follows. The modular coils are modeled as rectangles in cross section, 0.12m in height and 0.10m in width, with a 0.02m web at the center which separates each coil into two halves. There are 8 by 2 turns for each coil half; and each turn is modeled as a filament. This coil model resembles the proposed winding discussed in the Engineering Design Document.

We first note that the multi-filament coil model preserves the quasi-axisymmetry for the healed coils, M45h. Using effective ripple as a measure of quasi-symmetry, the results of NEO calculation based on VMEC equilibria show that the difference is less than 1.5% between single- and multi-filament models throughout the entire plasma volume. The effective ripple is 0.21% at r/a=0.5 for the single filament model, whereas it is 0.213% for the multi-filament model. Similarly, at r/a=0.9 it is 1.026% for the single-filament versus 1.029% for the multi-filament model. Also, the stability properties of the multi filament coils are similar to the single filament coils and that the multi filament coils are stable with respect to kink and ballooning modes.

PIES calculations indicate that the flux surfaces are similar in quality for both single- and multi-filament models of the healed coils (M45h) at the reference operating state. The finite build of the coils does not introduce extraneous resonant perturbations that destroy the properties of the healed coils, which are designed using the single filament model. Using the multi-filament coil set constructed, a PIES run is performed and the converged equilibrium is shown below Fig 3-9. The flux surface quality of the equilibrium actually appears better than the single filament coil case! The area of greatest improvement is the absence of the resonant m=18 deformation near the zero shear region.

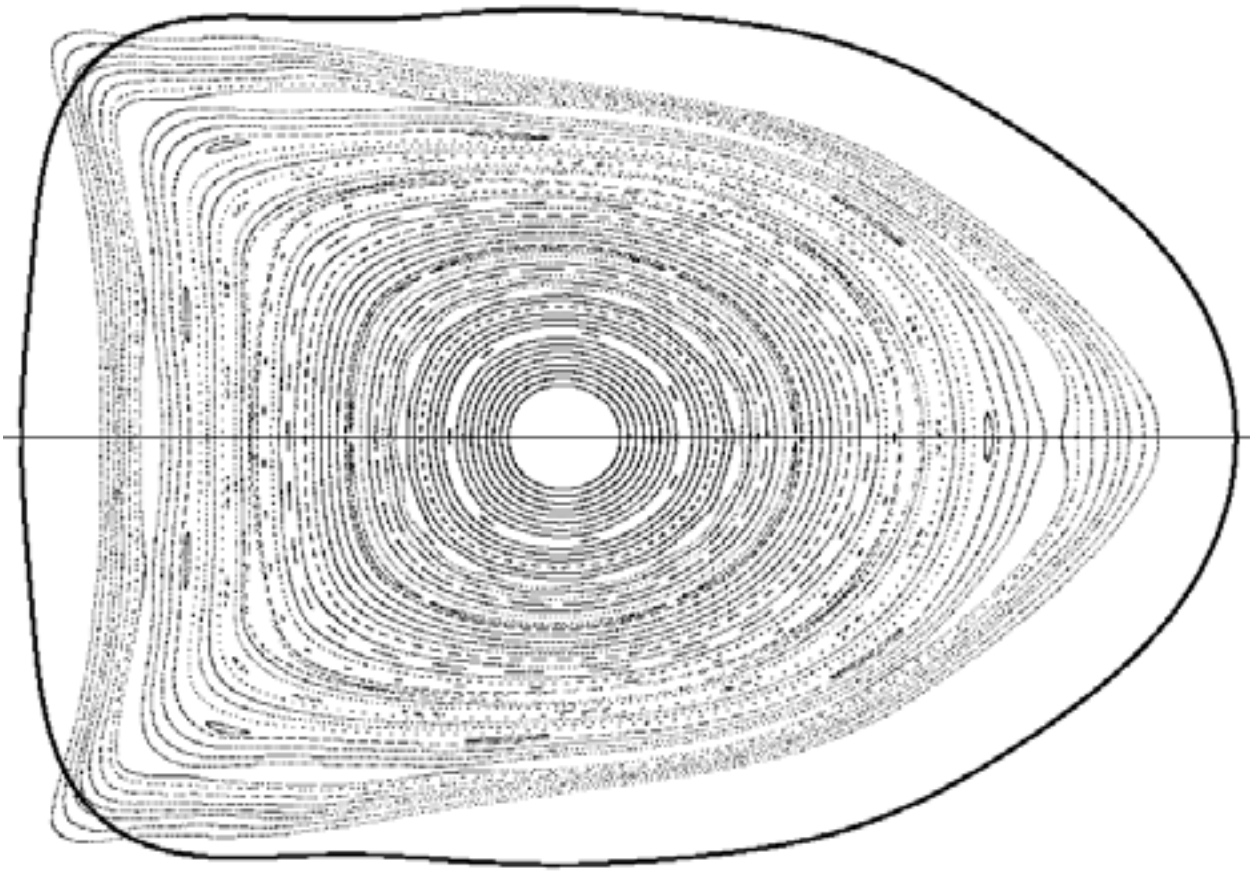

Figure 3-9. PIES equilibrium using the multi-filament healed coils (M45h) at β=4.1% The first wall boundary is shown as the solid line. This figure compares favorably to single filament equilibrium in Fig 3-7.

The improvement in flux surface quality in going from single filament to multi filament coil representations suggests that the remaining Poincare plots, which are all single filament calculations, may be conservative and that the finite coil build may improve flux surface quality for these configurations.

3.7.2 Vacuum Configurations with the Healed Coils.

The coil healing procedure considered only the full-pressure and full-current configuration; nevertheless, the healed coils produce plasma states at different pressure and

current with good flux surfaces over most of the plasma volume. Evidence of this will be shown in Chapter 9, where a simulated start-up sequence of equilibria at different operating times is presented. This section will present an analysis of a variety of vacuum states.

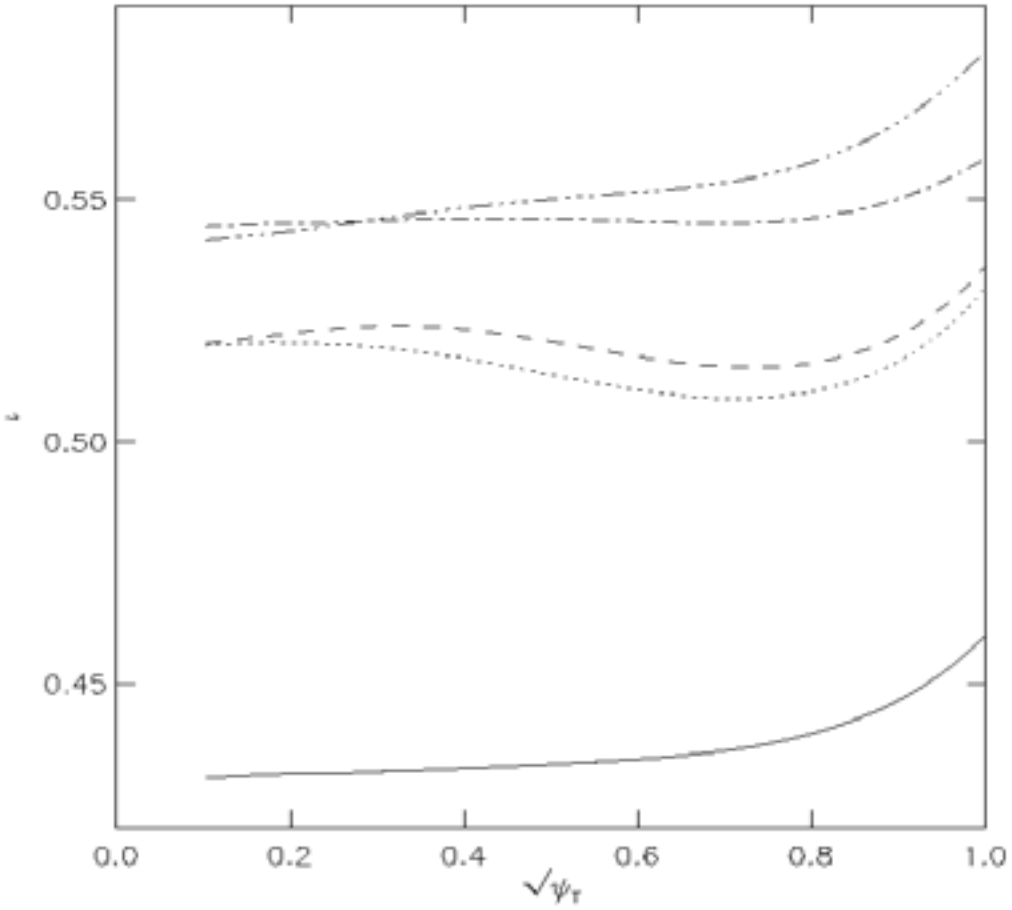

Figure 3-10. Rotational transform profiles for vacuum cases to be shown Fig 3-11 thru 3-15.

Various vacuum configurations are shown that confirm that good-flux surfaces may be obtained with the healed coils (M45h) for a number of cases. The Poincare plots shown in Figures 3-11 thru 3-15 show vacuum cases with different rotational transform profiles, varying from (i) 0.43 to 0.46; (ii) 0.52 to 0.53; (iii) 0.52 to 0.54; (iv) 0.54 to 0.56; and (v) 0.54 to 058. These profiles are shown in Fig 3-10. The adjustment of the rotational transform in the vacuum is achieved by variation of the coil currents. These plots all show good flux surfaces, to varying degrees, and indicate that a variety of starting points may be used to generate plasma evolution sequences which will ultimately reach the healed, operating configuration. In all of these plots the location of the first wall is shown as the thick solid line.

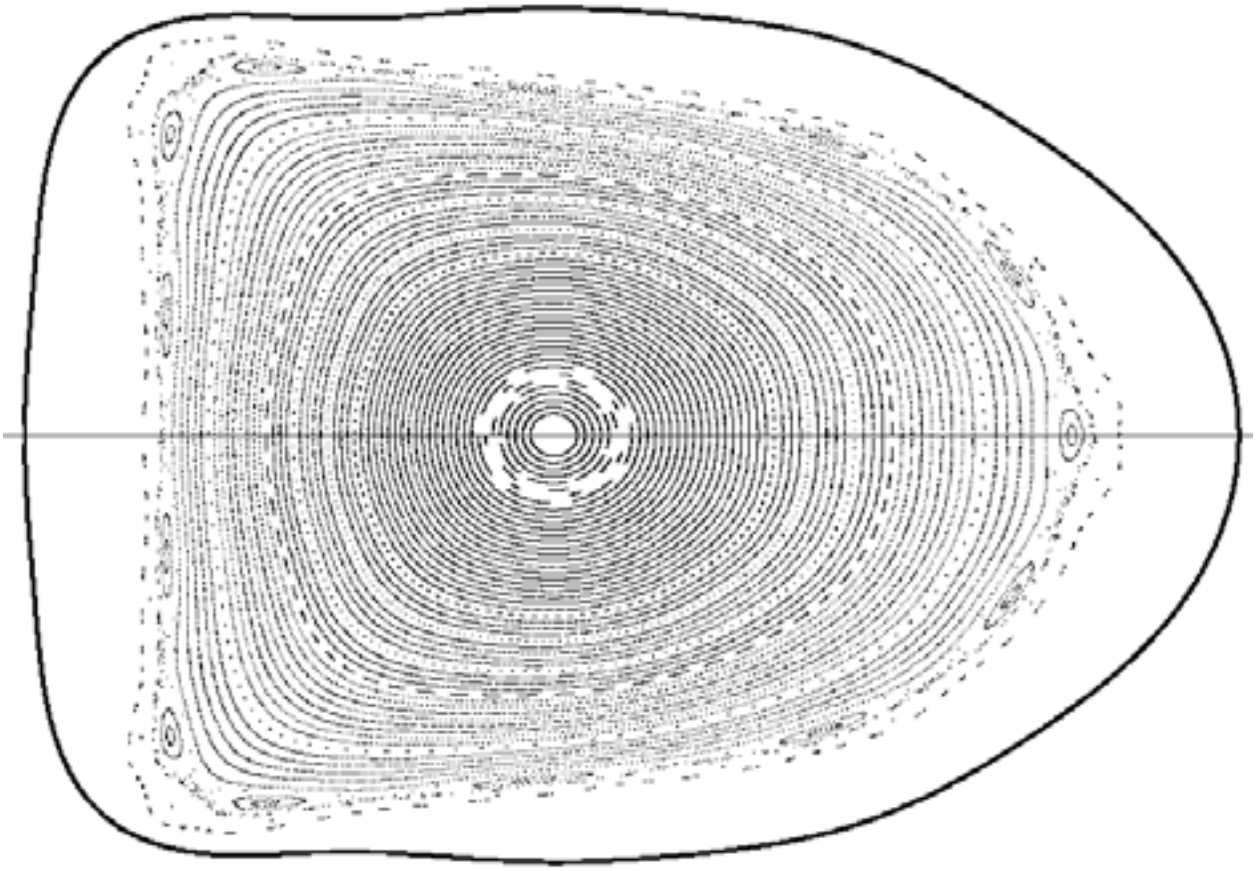

Figure 3-11. Vacuum configuration, ι=0.43-0.46, with healed coils (M45h). The first wall boundary is shown as the solid line.

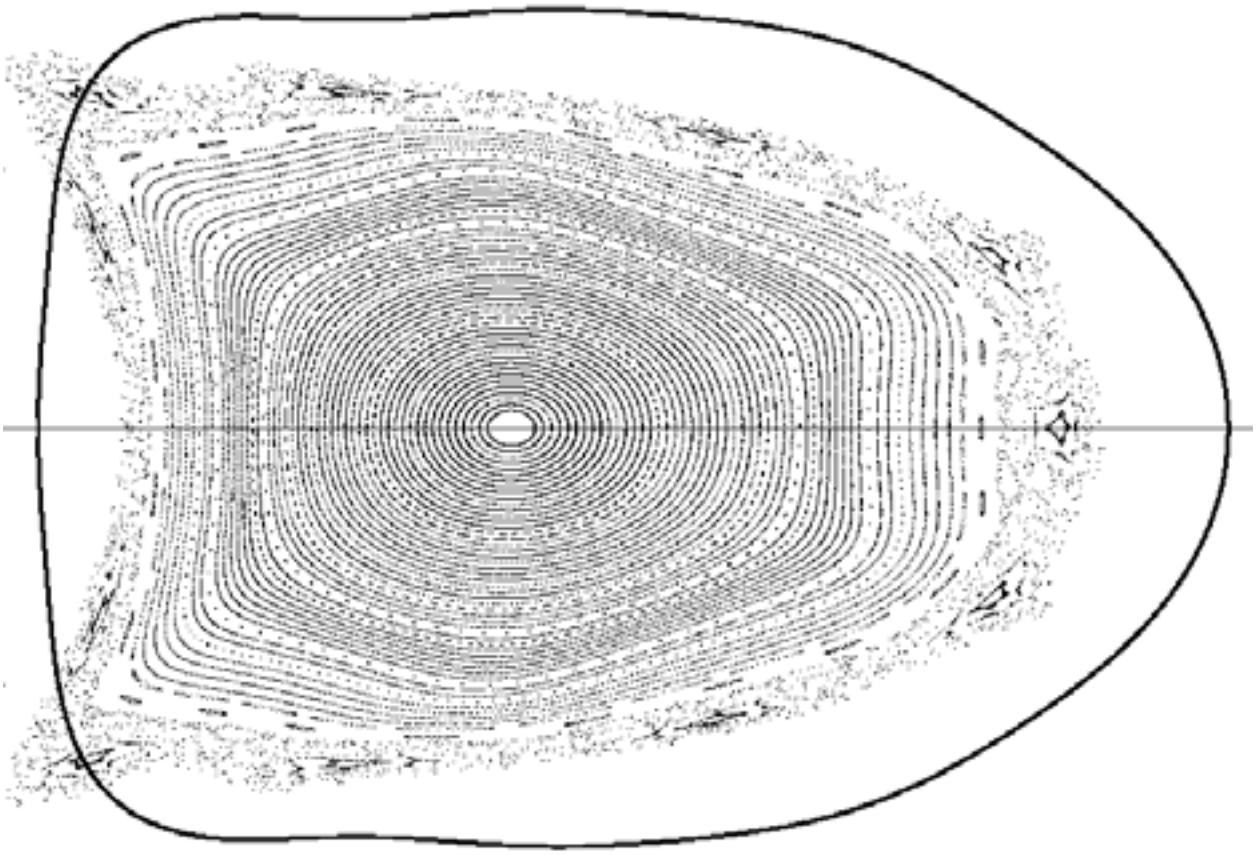

Figure 3-12. Vacuum configuration, ι=0.52-0.53, with healed coils (M45h). The first wall boundary is shown as the solid line.

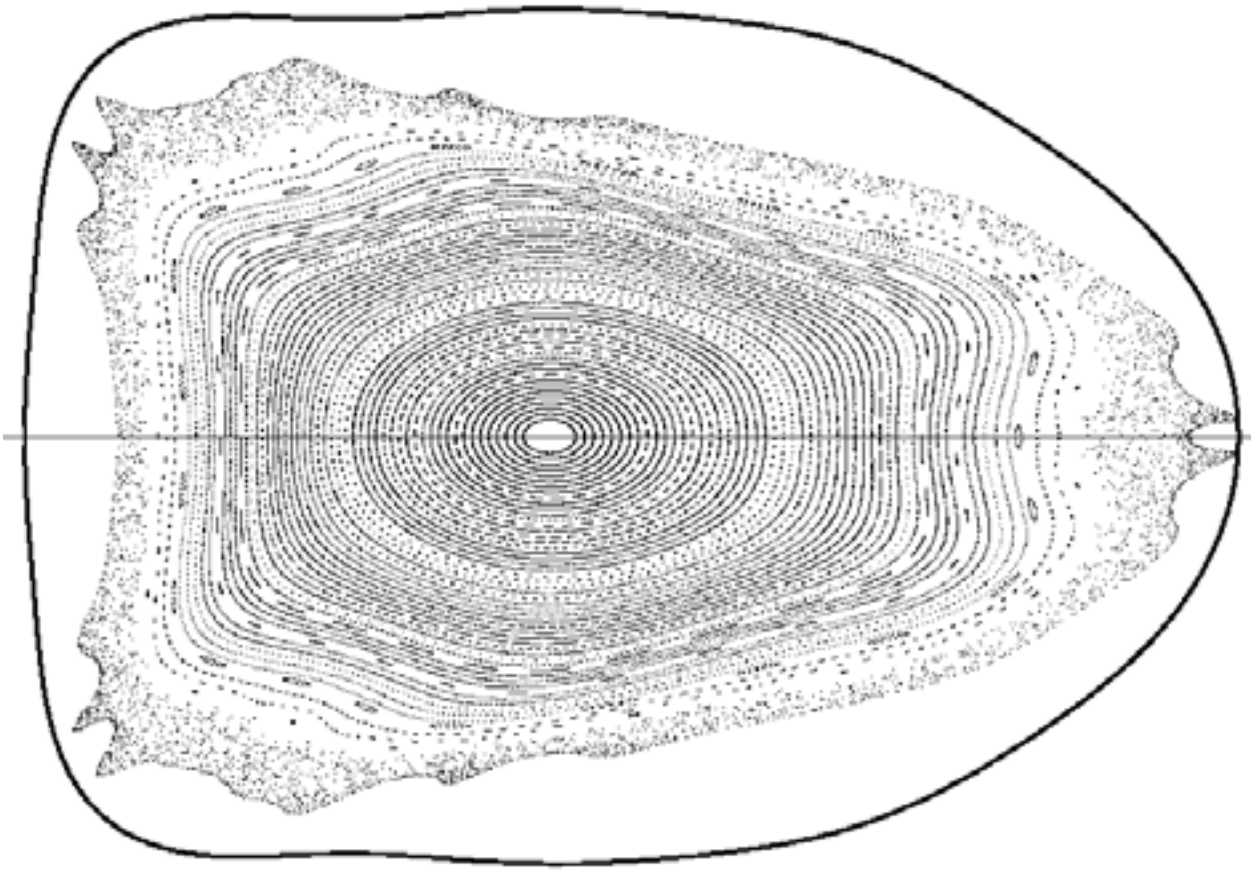

Figure 3-13. Vacuum configuration, ι=0.52-0.54, with healed coils (M45h). The first wall boundary is shown as the solid line.

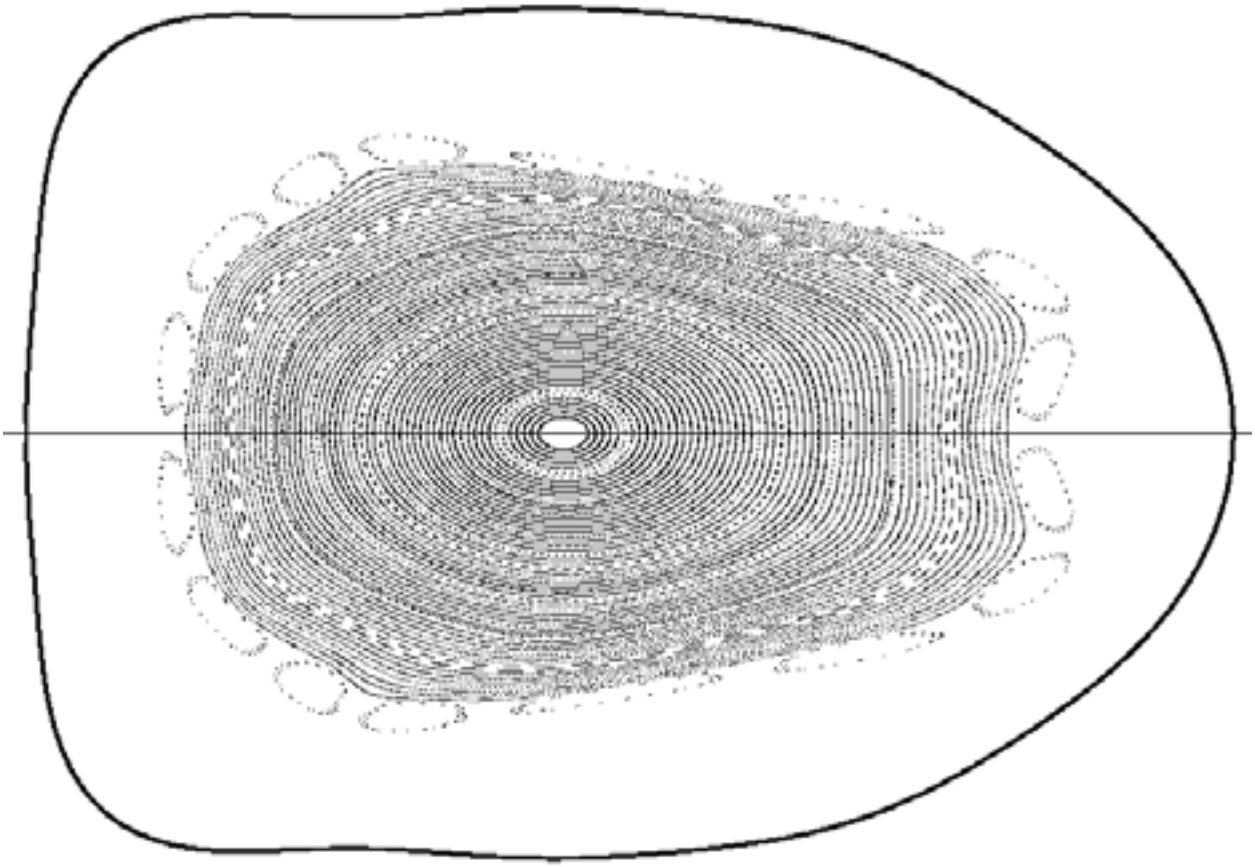

Figure 3-14. Vacuum configuration, ι=0.54-0.56, with healed coils (M45h). The first wall boundary is shown as the solid line.

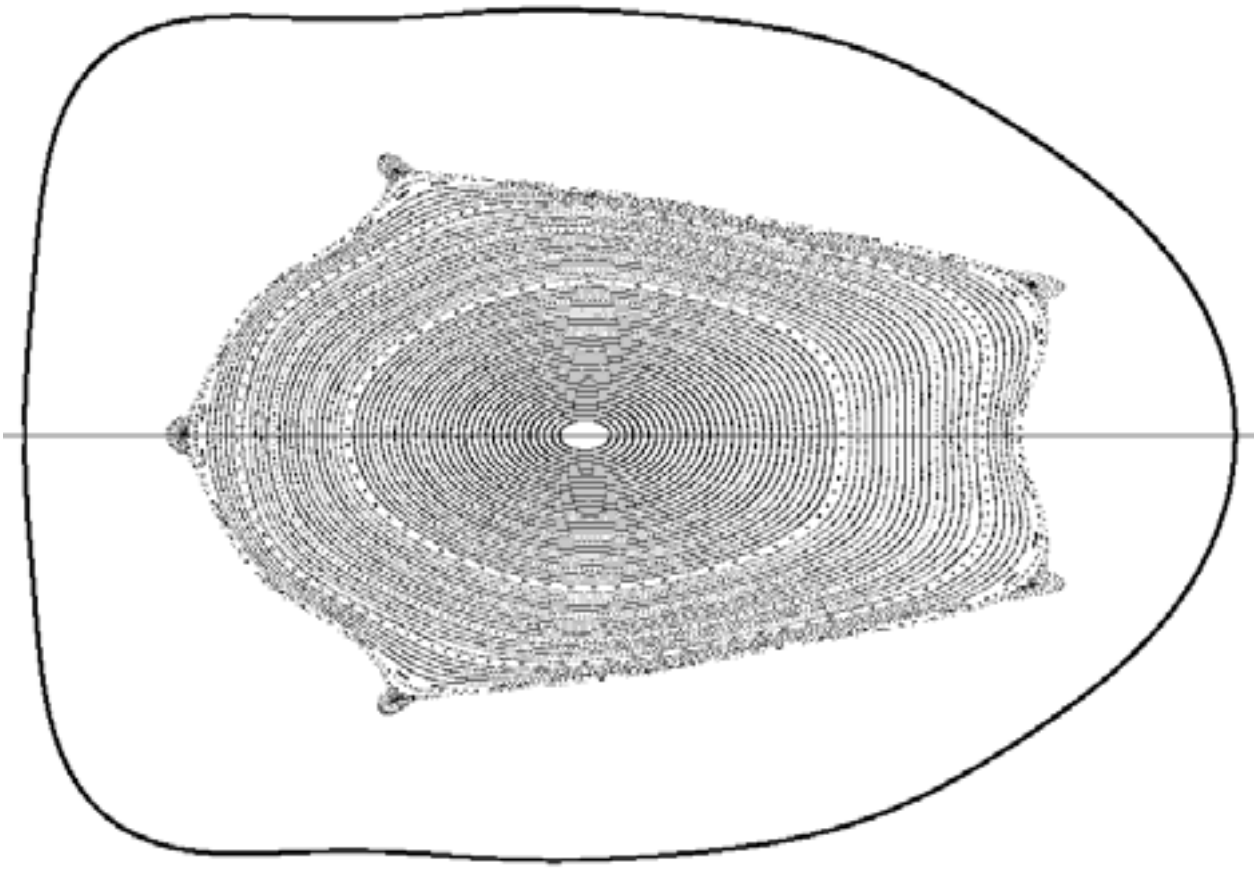

Figure 3-15. Vacuum configuration, ι=0.54-0.56, with healed coils (M45h). The first wall boundary is shown as the solid line.

3.7.3 Comparison of Healed Coils and Unhealed Coils at an Alternative Configuration.

The coils have been modified to heal the islands in the reference configuration. We find that, having reduced the amplitude of the resonant magnetic field components produced by the coils in this configuration, the flux surfaces are improved in other configurations as well. This is illustrated by the figure below, which shows the results of PIES calculations using the healed and unhealed coils for a configuration that arises in a startup scenario. The startup scenario is described in Chapter 9. The PIES calculations have been done for a time slice at 303 ms, with a β of 4.6%, and the configuration is stable to ballooning and kink modes. The upper half of the Poincare plot is for the healed coils, and the bottom half for the unhealed coils. There does exist an island in for the healed coils, but the flux surface quality of the healed coils for this configuration is far better than that of the unhealed coils. The PIES run for the unhealed coils is not converged, and continues to deteriorate as the calculation proceeds.

This plot shows that the healed coils (M45h) show improved flux surface quality in configurations other than the configuration for which the healing was performed. Note that this has been the general experience of coil healing, and was observed in healing of an earlier

candidate coil configuration, named 0907, presented at the Physics Validation Review (PVR) of NCSX.

The improvement of flux surface quality in going from a single filament coil model to a multi-filament model, and the fact the healed coils display better flux surface quality than the unhealed coils in a variety of configurations, is an encouraging observation of the healed coils.

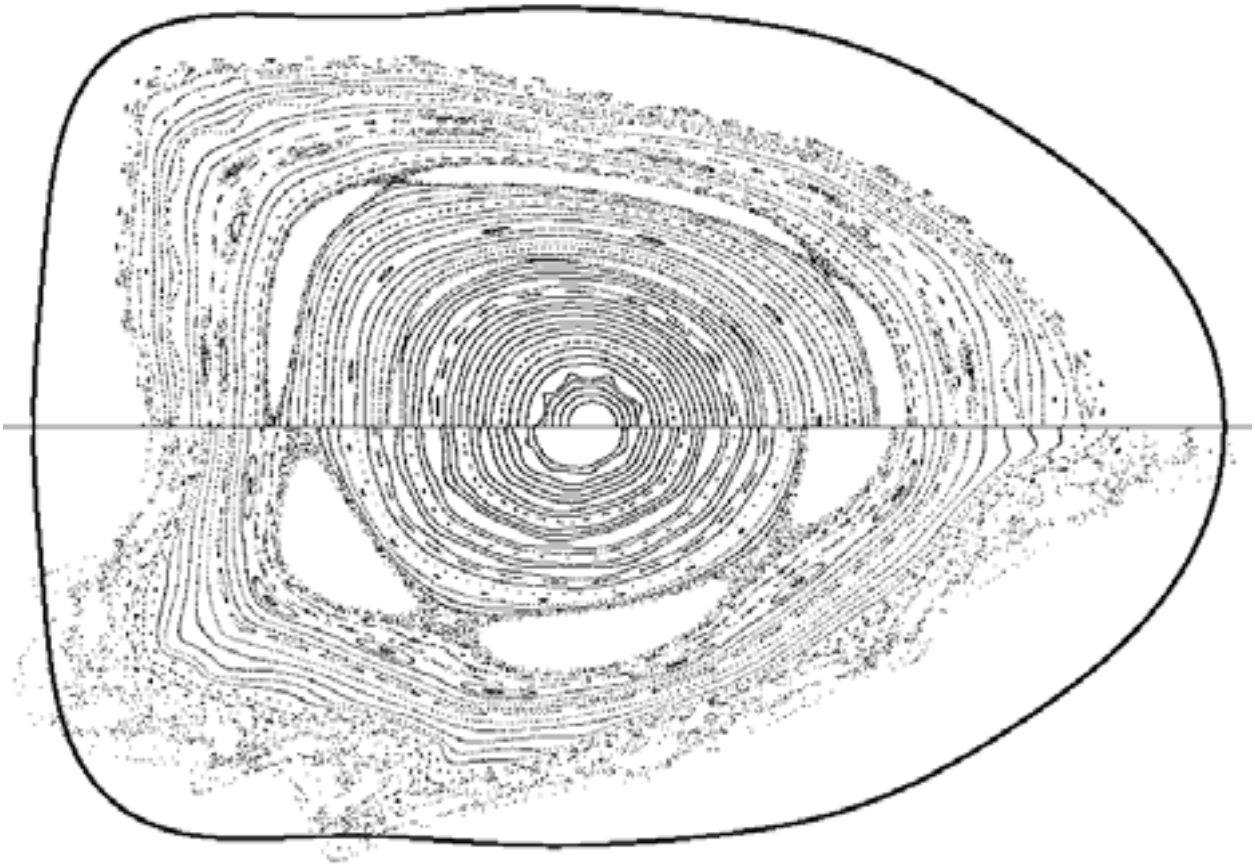

Figure 3-16. Startup evolution sequence time 303ms at =4.6% (see Chapter 9). The upper half is with the healed coils (M45h) and the lower half is with the unhealed coils (M45). The healed coils show significant improvement. The first wall boundary is shown as the solid line.

3.8 Neoclassical Healing of Magnetic Islands

3.8.1 Introduction

The purpose of this section is to estimate the effect of the neoclassical bootstrap current in reducing the width of magnetic islands produced by non-symmetric external field components in a “reversed shear” quasi-axisymmetric stellarator such as NCSX. It has been recognized for some time [47] that the bootstrap current, which can destabilize "neoclassical tearing modes" in

tokamaks, is stabilizing in a quasi-axisymmetric stellarator with outwardly increasing transform, i.e., positive dι/dr. There is experimental evidence for the neoclassical stabilizing effect from the LHD stellarator.[47a,47b] The magnitude of this effect depends on plasma collisionality, both through the dependence of the bootstrap current on the parameter ν_{*e} and through the role of finite parallel thermal conduction in limiting temperature flattening across the island.

In the present analysis, we employ the formalism of tokamak theory: the only stellarator-specific effect is an externally-imposed chain of magnetic islands with mode numbers corresponding to the dominant non-symmetric field "perturbation" in the NCSX configuration. For simplicity, we neglect two other effects, namely resonant Pfirsch-Schlueter currents and stabilizing resistive-interchange contributions, which are expected to be less important than the bootstrap current effect in the cases considered here.

3.8.2 Bootstrap Current Effect on Magnetic Islands

For cylindical tokamak geometry, including the bootstrap current density j_{bs}, the island width w in the weakly nonlinear regime [48,49,50] grows according to

$$(\mu_0/1.2\eta)\, dw/dt \;=\; \Delta' \;+\; 6.4\, (\mu_0 L_q/B_\theta)\, j_{bs}/w \qquad (3\text{-}20)$$

where Δ' is the usual tearing-mode stability quantity and $L_q = q/q'$. The numerical coeffficient 6.4 arises from calculating the applicable Fourier component of the current perturbation caused by zeroing the bootstrap current inside the magnetic island, i.e., within the area bounded by the island separatrix [51]. Writing

$$j_{bs} \;=\; -\; C_{bs}\, (\varepsilon^{0.5}/B_\theta)\, dp_e/dr \qquad (3\text{-}21)$$

where $\varepsilon = r/R$ and C_{bs} is a numerical coefficient of order unity which describes the dependences of the bootstrap current on the density and temperature profiles and on the collisionality parameter ν_{*e}, we obtain

$$(\mu_0/1.2\eta)\, dw/dt \;=\; \Delta' \;+\; 3.2\, C_{bs}\, \varepsilon^{0.5}\, \beta_{\theta e}\, (L_q/L_{pe})\, /w \qquad (3\text{-}22)$$

where $L_{pe} = -\, p_e/p_e'$. For the tokamak ($q' > 0$), the bootstrap current term is positive and can overcome a negative Δ' to produce unstable neoclassical tearing modes. Comparisons with experimental data from tokamaks have generally suggested a numerical coefficient somewhat smaller than 3.2 in this equation; for example, analysis of neoclassical tearing modes in TFTR gave a coefficient of 2.6 [52]. For present purposes, however, we will retain the somewhat larger theoretical coefficient.

The case of an island produced by the vacuum magnetic fields in a quasi-axisymmetric stellarator may be considered analogous to the case of a tokamak in which an island is produced by superimposing an external helical magnetic perturbation that is resonant on a magnetic surface within the plasma. If such a perturbation were imposed dynamically, then the plasma would respond initially (i.e., within ideal-MHD theory) by forming a helical sheet current on the resonant surface. This sheet current would then decay resistively, producing a magnetic island;

when the width of this island exceeds the very narrow resisitive layer of linear tearing-mode theory, it will be described by an appropriate generalization of the slow-growing tearing-mode theory. In the present context, we are interested in the case where the resonant helical perturbation has mode numbers m and n for which the tearing mode would be stable, i.e., for which Δ' is negative. (Accordingly, we henceforth write $\Delta' = - |\Delta'|$.)

It is straightforward to extend the theory of weakly nonlinear tearing modes [47] to include an externally driven island. Rather than introducing the external perturbation explicitly, it is more convenient simply to describe it in terms of the island width w_{ext} that would be produced after resistive relaxation of the currents on the scale-length of the island but without the bootstrap current effects. Adding the bootstrap current term as before, the island is found to evolve according to

$$(\mu_0/1.2\eta)\, dw/dt \;=\; - |\Delta'| \,(1 - w_{ext}^2/w^2) \;-\; 3.2\, C_{bs}\, \varepsilon^{0.5}\, \beta_{\theta e}\, (L_\iota/L_{pe})\, /w. \qquad (3\text{-}23)$$

Here we have also written $L_q = - L_\iota = - \iota'/\iota$, in order to use the quantity $\iota = 1/q$ that is more appropriate to a stellarator and to indicate that in this case the bootstrap term is stabilizing. For a high-m mode, to a very good approximation, we may use

$$\Delta' \;=\; - 2m / r\,. \qquad (3\text{-}24)$$

The "skin time" for resistive relaxation of w toward w_{ext} without bootstrap effects may now be estimated, namely $\tau_s = (\mu_0/1.2\eta)\, (2 w_{ext}\, r/m)$.

The bootstrap current term is seen to be inversely proportional to the island width w. This arises from the implicit assumption that density and temperature gradients are completely flattened across the magnetic island, thereby zeroing the bootstrap current within the island. Since electron thermal conduction is by far the fastest process of equilibration along field lines in high-temperature plasmas, bootstrap-current drive (or healing) of magnetic islands arises most effectively from the flattening of the electron temperature gradient, with flattening of the density gradient being less effective. Since in most practical cases (including the cases considered here) the electron temperature gradient provides the dominant contribution to the bootstrap current anyway, because the density profile is relatively flat, it is not unreasonable to employ the full bootstrap current in calculations such as these, but it should be recognized that this may give an over-estimate of the bootstrap-current effect on magnetic islands in some cases.

For very narrow islands, however, the path length along the helical field lines becomes very long, and finite (as distinct from effectively infinite) electron thermal conduction along the field lines will prevent the electron temperature from flattening fully across the island, thereby reducing even the most effective process of bootstrap-current island drive or healing. This effect is introduced into the theory [51] by modifying the bootstrap current term as follows:

$$1 / w \;\;\Rightarrow\;\; w / (w^2 + w_0^2\,) \qquad (3\text{-}25)$$

where we have defined a "critical island width" w_0, namely

$$w_0 \;=\; 5.1\,(\chi_\perp / \chi_{//})^{0.25}\,(\,R L_\iota / m\iota\,)^{0.5}. \qquad (3\text{-}26)$$

Here, $\chi_\perp$ and $\chi_{//}$ are the perpendicular and parallel thermal diffusivities, which control the degree to which the temperature is flattened across the island.

Setting dw/dt = 0, we then find the following relation to describe the actual island width w in terms of w_{ext} with bootstrap current effects included:

$$w_{ext}^2 / w^2 \;=\; 1 \;+\; 2 w_{bs}\, w\,/(w^2 + w_0^2\,), \qquad (3\text{-}27)$$

where we have introduced an island width characterizing the bootstrap current effect, namely

$$w_{bs} \;=\; 1.6\, C_{bs}\, \varepsilon^{0.5}\, \beta_{\theta e}\, (L_\iota / L_{pe}) \,/\, |\Delta'|. \qquad (3\text{-}28)$$

3.8.3 Assumed NCSX Parameters and Profiles

We have assumed the following parameters for the reference NCSX high-beta plasma:

$$\begin{aligned} &R \;=\; 1.4 \;\text{m} \\ &a \;=\; 0.32 \;\text{m (average)} \\ &\langle\beta\rangle \;=\; 4.2\,\% \\ &B_0 \;=\; 1.2 \;\text{T} \\ &\langle n_e\rangle \;=\; 5.8 \times 10^{19}\;\text{m}^{-3}. \end{aligned} \qquad (3\text{-}29)$$

We have used density and temperature profiles that correspond very closely to those resulting from transport calculations for NCSX [53], namely:

$$\begin{aligned} n_e(r) \;&=\; 7.8\,(1 - r^2/a^2)^{0.35} \qquad (10^{19}\;\text{m}^{-3}) \\ T_e(r) \;&=\; 2.8\,(1 - r^2/a^2)^{1.35} \qquad (\text{keV}) \\ T_i(r) \;&=\; 1.9\,(1 - r^2/a^2)^{0.75} \qquad (\text{keV}). \end{aligned} \qquad (3\text{-}30)$$

The use of profiles that are parabolas raised to exponents α_n and α_T facilitates the calculation of the bootstrap current from the relevant theory. We have used an iota profile for the reference configuration for which the iota = 0.6 surface falls at r/a = 0.8 (see Section 3.1). The only other quantity needed from the iota profile is the local shear length, which for this profile is given by $L_\iota / a \;=\; 0.7$. It should be noted that the shear length L_ι may be longer for iota profiles that flatten or decrease toward the plasma edge.

3.8.4 Bootstrap Current Magnitude

To evaluate the bootstrap current term, i.e., the characteristic island width w_{bs}, it is essential to have a good estimate for the constant C_{bs}, since this can vary appreciably depending on profiles and on plasma collisionality. For present purposes, we have assumed the profiles

given above and have employed the Hinton-Rosenbluth neoclassical theory for the "banana/plateau transition" [54], taking $Z_{eff} = 1.5$. We have allowed for $T_i \neq T_e$ and have included both the ∇T_e and ∇T_i contributions to the bootstrap current. We obtain collisionality parameters (at the resonant surface r/a = 0.8) given by $\nu_{*e} = 0.49$ and $\nu_{*i} = 0.27$. For the profiles assumed and for these collisionality parameters, we than obtain $C_{bs} = 1.37$, which gives

$$w_{bs} / a = 0.28 . \tag{3-31}$$

In practical units, the value of C_{bs} found here corresponds to a bootstrap current density at the resonant surface r/a = 0.8 given by $j_{bs} = 60$ A/cm^2. This value is close to the peak of the bootstrap current density profile in this case, because of the strong local pressure gradient and modest collisionality in the region of the resonant surface. This value agrees reasonably well with other calculations of the bootstrap current density in the NCSX reference configuration (see Section 3.2).

For the case considered here, the major contribution to the bootstrap current arises from the electron temperature gradient. This is partly because the density gradient is relatively small and partly because the coefficient in the transport matrix that multiplies the electron temperature gradient falls off less strongly with collisionality than does the coefficient multiplying the density gradient. The ion temperature gradient is found to make only a small contribution to the bootstrap current.

3.8.5 Critical Island Width w_0

To evaluate the critical island width, w_0, we need estimates for the perpendicular and parallel electron thermal diffusivities. We obtain an estimate for $\chi_\perp$ from its relation to the energy confinement time τ_E. Using $\tau_E \approx a^2 / 4\chi_\perp$ together with the empirically projected energy confinement time in NCSX of 25 msec, we obtain an estimate $\chi_\perp \approx 1.0$ m^2/s.

Obtaining a good estimate for $\chi_{//}$ is trickier. We start by calculating the Spitzer parallel electron thermal diffusivity at the resonant surface; this gives $\chi_{//}^{Sp} \approx 2.9 \times 10^9$ m^2/s. If we use this value in the expression for w_o, we would obtain $w_0 / a \approx 0.02$. However, at low collisionality, the electron mean-free-path typically exceeds the parallel wavelength along the helical perturbations. In such cases, the use of Spitzer thermal diffusivity may lead to unphysically large parallel heat fluxes, and thermal diffusion must effectively be replaced by thermal convection, according to the relationship $\chi_{//} \nabla_{//}^2 T_e \Rightarrow v_{the} \nabla_{//} T_e$, where v_{the} is the electron thermal velocity. The quantity $\nabla_{//}$ is the inverse parallel wavelength along the helical perturbation, which depends on the island width w and can be estimated as $\nabla_{//} \approx (mw/R)\, d\iota/dr = m\iota w / RL_\iota$. Since $\chi_{//}$ appears only to the one-quarter power, it is not necessary to retain this explicit dependence on the island width w and so, for present purposes, we simply estimate it as $w/a \approx 0.05$. For the "effective" thermal diffusivity in this convection-limited regime, we obtain $\chi_{//}^{eff} \approx 7.2 \times 10^7$ m^2/s. If we use this value in the expression for w_0, we would obtain $w_0 / a \approx 0.05$ (validating our estimate used to obtain $\chi_{//}^{eff}$).

Without more theoretical work, it is not obvious which value to use for w_0. Almost certainly, the Spitzer thermal diffusivity will overestimate parallel heat transport at low

collisionality. On the other hand, fast electrons may still be able to equilibrate the temperature at a rate faster than that given by convection at the thermal speed. Accordingly, it might be appropriate to take a range $w_0/a = 0.03 - 0.04$. In the calculation of the bootstrap island effect given below, we have simply chosen an intermediate value, namely:

$$w_0/a \approx 0.035. \tag{3-32}$$

It has been pointed out [55] that islands of width less than w_0 would not be expected to have a seriously deleterious effect on confinement because transport from one side of the island to the other along the direct path is already larger than transport along the path that follows the helical field lines. For the high-β NCSX reference case, this effect would apply only to islands with widths less than about 1 cm. However, the effect (unlike the bootstrap current) does not depend on the plasma beta-value and it increases strongly with higher collisionality, so it should apply particularly to low-temperature pre-heated plasmas. The Spitzer parallel thermal diffusivity scales as $T_e^{2.5}$, so a reduction in the temperature at the resonance surface to 100 eV (from 700 eV in the high-β plasma) would result in an increase in w_0/a to about 0.08. (Since parallel thermal convection scales much more weakly with electron temperature than thermal diffusivity, we find that the Spitzer diffusivity would be the operative process in this case.) This result suggests that in low-temperature ohmic plasmas in NCSX, islands at the iota = 0.6 surface as large as about 2.5 cm may not have a seriously detrimental effect on confinement.

3.8.6 Results for NCSX Reference Case

The actual island widths w for a range of possible "externally-produced" island widths w_{ext} are given in Table 3-2. For this calculation, we have taken $w_{bs}/a = 0.28$ and a value $w_0/a = 0.035$ (see the preceeding discussions). For external islands with widths in the range 2 - 6 cm (i.e., 6 - 18 % of the minor radius), the bootstrap current reduces the island width by almost a factor-of-three.

w_{ext} (cm)	w (cm)
1.0	0.41
2.0	0.70
3.0	1.00
4.0	1.34
5.0	1.73
6.0	2.19

Table 3-2. Neoclassical bootstrap-healed island widths w for various externally-generated island widths w_{ext} at the iota = 0.6 surface in the reference NCSX high-β configuration

3.8.7 Conclusions Concerning Neoclassical Healing

The depletion of bootstrap current within the island causes a substantial reduction in the width of the magnetic island caused by the dominant non-symmetric field "perturbation" in NCSX. Specifically, for the 4%-beta reference NCSX configuration, the bootstrap current

should reduce the width of the m/n = 5/3 islands at the iota = 0.6 surface by almost a factor-of-three.

The bootstrap current in NCSX is sufficient for this purpose despite the relatively high collisionality of the plasma, which puts the island region (where $\nu_{*e} \approx 0.5$) in the "banana-plateau transition", rather than "pure banana", regime of neoclassical transport. For the cases considered, the main contribution to the bootstrap current comes from the electron temperature gradient, rather than the density gradient. The key element in ensuring sufficient bootstrap current is a relatively high value of the local $\beta_{\theta e}$ at the resonant surface together with a relatively steep local electron pressure gradient.

3.9 Suppression of Magnetic Islands by Plasma Flow

3.9.1 Introduction

Resonant magnetic field perturbations can be shielded out at rational surfaces by plasma flow.[56,57] This effect is believed to play a major role in reducing the vulnerability of present day tokamaks to resonant field errors. The effect has been studied systematically in tokamak experiments where externally imposed magnetic field perturbations have been varied and their penetration threshold determined.[58,59,60] The shielding effect can ameliorate the problem of magnetic island formation also in stellarators, suppressing islands caused by externally imposed magnetic fields, or by the magnetic fields produced by pressure driven currents in the plasma itself. We will see in this section that, for appropriate startup scenarios, the flow suppression of resonant field perturbations is predicted to be stronger in NCSX than in tokamaks of comparable size. This could be helpful in reducing the vulnerability to field errors produced by finite tolerances in the construction and placement of the magnetic field coils, and also allows larger tolerances in the modification of the coil design to suppress islands. The effect is not strong enough to rely on it entirely for the suppression of the relatively large resonant perturbations arising naturally in coil design, and flux surface targeting such as that described in Section 3.6 is a prudent step in the design of the coils.

NCSX is predicted to have a strong toroidal flow, driven by the self-consistent ambipolar electric field, and this flow is predicted to provide strong shielding of rational surfaces. Tokamaks are most vulnerable to field error penetration just before the neutral beams are turned on, when the flow is diamagnetic, and studies of field error penetration in tokamaks focus particularly on ohmic discharges. In contrast to tokamaks, NCSX is predicted to have a large flow even in the absence of external momentum input. NCSX also has an advantage that neutral beam ions can be captured earlier in the discharge because flux surfaces exist at the outset. Further, the externally generated transform provides a flexibility not available in tokamaks in adjusting the _ profile to avoid low order rational surfaces early in the discharge, when the vulnerability to resonant field error penetration is greatest. These considerations suggest that flow effects on resonant field suppression will be stronger in NCSX than in a comparable tokamak, providing reduced vulnerability to resonant field errors. On the other hand, because coil design for stellarators does not have a symmetry principle to fall back on, stellarator coils designed without the explicit targeting of resonant field error reduction may have relatively large resonant field errors. The net effect must be assessed by a quantitative estimate of the

penetration threshold for resonant magnetic field perturbations and a comparison with calculated resonant fields produced by the coils. We discuss such a comparison for the NCSX coils in this section.

3.9.2 Penetration of Resonant Fields

In the presence of a sufficiently strong plasma flow, a localized current is induced at rational surfaces that shields out resonant magnetic perturbations. While shielding out a large fraction of the resonant field perturbation, the induced current at the same time interacts with the remnant of the resonant field at the rational surface to produce a **j** x **B** torque there. This electromagnetic torque opposes the motion of the plasma at the rational surface, and acts to slow the flow. When the resonant perturbation is sufficiently large, the torque is large enough to locally suppress the plasma flow, allowing the resonant perturbation to fully penetrate the rational surface.

In a tokamak, the electromagnetic torque is opposed by a viscous torque produced by the plasma flow. The flow is diamagnetic in an ohmic tokamak, and is driven by the neutral beams in a neutral beam heated tokamak with unbalanced beams. The threshold for resonant field penetration is determined by the relative magnitude of the electromagnetic torque and the viscous torque, and is significantly higher in a tokamak where the flow is driven by neutral beams.

In a stellarator, the threshold for penetration of resonant field perturbations will also be determined by the relative magnitudes of the electromagnetic torque and of the torques associated with the plasma flow. As we will discuss in Section 3.9.3, the electromagnetic torque in a stellarator is comparable to that in a tokamak. The flow driven by the ambipolar field in NCSX is predicted to be quite large, comparable in magnitude to neutral beam driven flows in tokamaks. We can use penetration thresholds observed in neutral beam heated toakamk experiments to estimate the expected thresholds for NCSX. The electromagnetic torque will be discussed in Section 3.9.3. The torques associated with the plasma flows will be discussed in Section 3.9.4. In Section 3.9.5 we will estimate the expected penetration threshold in NCSX.

The torques are a function of the flow velocity at the rational surface. In particular, once a resonant magnetic field perturbation has fully penetrated a rational surface, if the perturbation magnitude is then reduced, the threshold perturbation magnitude below which plasma rotation is restored is lower than the perturbation threshold initially required to induce penetration in a rotating plasma. This suggests that it may be desirable in NCSX to use startup scenarios in which the vacuum rotational transform is initially relatively flat and lies above the low order resonances. As shear is introduced and the transform on axis is reduced, the rational surfaces enter the plasma from the magnetic axis. Because the magnitude of the resonant perturbations scale radially as r^{m-1} near the axis, where m is the poloidal mode number, the surfaces are initially unbroken and rotating with the bulk plasma motion.

3.9.3 Electromagnetic torque.

Consider the case where a small perturbation of the magnetic field is turned on in a plasma that initially has good flux surfaces. This corresponds, for example, to a scenario where the rotational transform is manipulated during startup so that the rational surfaces enter the plasma from the magnetic axis. Nonresonant Fourier components of the perturbation introduce small ripples in the flux surfaces but do not break the flux surfaces. To see this, express the unperturbed magnetic field in magnetic coordinates: $\mathbf{B}_0 = \nabla\Psi_0 \times \nabla\theta + \iota\nabla\Psi_0 \times \nabla\varphi$, where $\mathbf{B}_0$ is the unperturbed field, and Ψ_0 is an unperturbed flux function satisfying $\mathbf{B}_0\cdot\nabla\Psi_0 = 0$. Write $\mathbf{B} = \mathbf{B}_0 + \boldsymbol{\delta}\mathbf{B}$, $\Psi = \Psi_0 + \delta\Psi$. To first order $\mathbf{B}_0\cdot\nabla(\delta\Psi) = -\boldsymbol{\delta}\mathbf{B}\cdot\nabla\Psi_0$. In magnetic coordinates, this can be expressed

$$\mathbf{B}_0\cdot\nabla\varphi \left(\partial\, \delta\Psi / \partial\varphi + \iota\, \partial\, \delta\Psi / \partial\theta \right) = -\boldsymbol{\delta}\mathbf{B}\cdot\nabla\Psi_0 . \qquad (3\text{-}33)$$

Dividing by $\mathbf{B}_0\cdot\nabla\varphi$ and Fourier transforming, we get

$$(n - \iota\, m)\, \delta\Psi_{nm} = -(\boldsymbol{\delta}\mathbf{B}\cdot\nabla\Psi_0 / \mathbf{B}_0\cdot\nabla\varphi)_{nm}. \qquad (3\text{-}34)$$

The nonresonant Fourier components just introduce small ripples in the flux surfaces. If a resonant Fourier component is present (one satisfying $n = \iota\, m$), the flux surface is broken and a magnetic island is produced.

In an ideal plasma, reconnection is prohibited and the flux surfaces cannot be broken. A surface current is induced at the rational surface that shields out the resonant component of $\boldsymbol{\delta}\mathbf{B}\cdot\nabla\Psi_0 / \mathbf{B}_0\cdot\nabla\varphi$. In the absence of plasma flow, the presence of a small resistivity causes the surface current to decay, and allows the resonant field to penetrate the rational surface. If flow is present at the rational surface, a localized current continues to be induced which partially shields out the resonant component of the field. The induced current at the rational surface interacts with the resonant magnetic field to produce a net torque. The torque is increased somewhat, relative to its value in cylindrical geometry, by mode coupling effects due to finite aspect ratio and to plasma shaping. The mode coupling effect has been studied experimentally in COMPASS-D and in DIII-D by independently varying the currents in different external coils, and measuring the penetration threshold as a function of the harmonic content of the perturbing field.[60] The strongest shaping components in NCSX are axisymmetric, and we can expect these axisymmetric shaping components to dominate the mode coupling.

The above considerations suggest that, for a given amplitude of the resonant field, the electromagnetic torque in NCSX will be roughly the same as that in a tokamak with the same parameters (including the rotation frequency). In comparing with a tokamak shot, we will use a DIII-D shot in which the plasma boundary has the same axisymmetric elongation as that of NCSX.

In comparing the electromagnetic torque with that in a tokamak, we will want to do the comparison for perturbations having different mode number. The theory for the linear visco-resistive regime for a fluid model in cylindrical geometry [61] finds that, for a given plasma rotation frequency, the penetrated flux scales as $1/n$, while the torque for a given penetrated flux scales as n, so that the effects cancel out and the penetration threshold is independent of n.

In comparing with DIII-D, we will also be concerned with the scaling with minor radius. This will be discussed in Section 3.9.5.

3.9.4 Torque Produced by the Plasma Flow

In a tokamak, the plasma flow exerts a viscous force at the rational surface that opposes the electromagnetic torque. The viscous force may be estimated as $\rho\mu\nabla^2 v$, where ρ is the mass density, μ is an anomalous viscosity, and v is the fluid velocity. The momentum confinement time, a^2/μ, is generally found to be approximately equal to the anomalous energy confinement time. In an ohmic tokamak, the flow is believed to be produced by plasma diamagnetism. In a neutral beam heated tokamak with unbalanced beams, there is a much stronger flow driven by the neutral beams.

When a resonant perturbation is imposed on a rotating plasma, the resulting electromagnetic force slows the plasma rotation at the rational surface. The opposing viscous force increases as the velocity at the rational surface decreases. Initially, the plasma slows continuously as the magnitude of the resonant perturbation is increased. When the velocity slows to about half its initial value, there is an abrupt transition to a locked mode with a significantly increased island width.[61, 60]. To evaluate the force associated with the plasma flow in NCSX relative to the viscous force in a tokamak, we calculate the forces when the plasma velocity is half its natural value. (That is, half the value it achieves in the absence of the electromagnetic force.)

In a stellarator, the transport is not intrinsically ambipolar, and there is a radial current in the absence of an electric field. A self-consistent ambipolar electric field is produced that zeroes out the radial current, and the electric field produces an **E x B** flow. As the flow velocity is reduced at the rational surface by an electromagnetic torque, a radial current reappears, producing a **j x B** torque that opposes the electromagnetic torque. There is also a viscous torque produced by the **E x B** flow that opposes the electromagnetic torque.

To evaluate the torques associated with plasma flow in NCSX, we consider a reference case whose transport properties are discussed in detail in Chapter 7, with $\langle\beta\rangle = 4\%$, $n_e = 6 \times 10^{19}$ m^{-3}, min. $\nu_i^* = 0.25$. We will compare with a DIII-D reference case[59] having $\langle\beta\rangle \approx 3.7\%$, $n_e \approx 5 \times 10^{19}$ m^{-3}, κ=1.8 and a rotation frequency of $f/n \approx 12$ kHz with about 5MW of injected neutral beam power.

We evaluate the torques in NCSX at the $\iota = 0.6$ rational surface. The ambipolar potential there is calculated to be about 20 kV/m in the reference case, corresponding to an ambipolar toroidal flow velocity of about 85 km/sec. The corresponding rotation frequency is about 10 kHz. If the toroidal velocity is slowed to half this value by the electromagnetic torque, the radial current is approximately 3 A/m^2. The current exerts a torque density at the rational surface of 15 Nt, in a direction which opposes the electromagnetic torque. The total torque exerted directly by the radial current is obtained by integrating the torque density across the magnetic island width, or across the visco-resistive layer width[61], whichever is larger. The island width in the rotating plasma is calculated to be comparable to the layer width for NCSX parameters. There is also a viscous torque exerted by the plasma flow, approximately given by $4\pi^2 r R^2 \rho\mu\left[\partial v/\partial r\right]$,

where $\left[\partial v/\partial r\right]^{\pm}$ is the jump in the radial derivative of the fluid velocity across the layer. Because of the narrowness of the layer width, the viscous torque is estimated to be much larger than the torque exerted directly by j_r.

The viscous torque can be written as $2\pi^2 rR^2 \rho\mu v_0 / l$, where v_0 is the toroidal velocity corresponding to the ambipolar potential and l is the scale length of the velocity gradient near the rational surface. The velocity gradient is determined by the steady-state solution of the momentum diffusion equation, with the torque exerted by the radial current as a source term. We approximate the v dependence of j_r as linear, $j_r \approx \alpha(v - v_0)$ where α is chosen to match the calculated radial current when $v = v_0/2$. The velocity near the rational surface satisfies the equation $\rho\mu d^2(v - v_0)/dr^2 = \alpha B_p (v - v_0)$, with the boundary condition that $v = v_0/2$ at the rational surface. To estimate μ we use an estimate of 25 ms for the confinement time for our NCSX plasma. Substituting in the parameters of our NCSX reference case we calculate a scale length of 6 cm for the velocity gradient.

We are interested in the ratio of the viscous torque to the electromagnetic torque. The $4\pi^2 rR$ factor corresponding to the area of the rational surface factors out of the numerator and denominator, as does the factor of R multiplying the force to give the torque. To compare the viscous force density in the NCSX case with that in the DIII-D reference case we consider the relative values of $\rho\mu v/l = 2\pi R\rho\mu f/l$, where l is the velocity gradient scale length and f is the toroidal rotation frequency. The ratio of R is 1.7 / 1.4 = 1.2. The ratio of the densities in the two cases is 5 / 6 = 0.83. For an energy confinement time on DIII-D of 120 ms, we estimate $\mu \approx 3$ m^2 / sec. This compares with a value of 4.4 m^2 / sec assumed for the NCSX calculation, giving a ratio of 0.69. The ratio of the frequencies is 1.2. We take the velocity gradient scale length in DIII-D to be comparable to the minor radius = 0.6 m, while that in NCSX has been calculated to be roughly 0.06 m. The viscous force density in DIII-D is calculated to be about 0.08 that in NCSX.

3.9.5 Threshold for Penetration of Resonant Perturbations

Resonant magnetic perturbations are predicted to penetrate the rational surface when the associated electromagnetic torque exceeds the viscous torque exerted by the plasma flow. To calculate a predicted penetration threshold for NCSX, we use the theoretically predicted scaling with minor radius[61] to scale the observed threshold in the DIII-D reference case to that of a tokamak with the same minor radius as NCSX. The minor radius of the two devices differ by about a factor of 2. The density, temperature, magnetic field, and rotation frequency of the DIII-D reference case are approximately the same as those predicted for the NCSX reference case. The major radius is also approximately the same. The electromagnetic torque in NCSX is predicted to be approximately the same as that in the equivalent tokamak (Section 3.9.3). The torque associated with the flow in NCSX differs from that in an equivalent tokamak due to the difference in the predicted velocity gradient scale length, giving a viscous force about a factor of 2.5 times that in the equivalent tokamak. The electromagnetic force scales like B_r^2, so the penetration threshold is about 1.6 times that in the equivalent tokamak.

For a given value of the plasma parameters and of f, the theory in the visco-resistive regime[61] predicts that the ratio of the electromagnetic to the viscous force in a tokamak scales as $a^{2/3}R^{-7/3}$. The penetration threshold therefore scales as $a^{-1/3}R^{7/6}$. This predicts that a tokamak with the dimensions of NCSX and the same plasma parameters and rotation frequency as the DIII-D reference case should have approximately the same penetration threshold. (The scaling factor is 0.97.) The experimentally observed penetration threshold in the DIII-D reference case is $B_{r21}/B \approx 4\text{x}10^{-4}$. Because of the shorter velocity gradient scale length predicted for NCSX, due to the strong $j_r B_p$ torque, the penetration threshold for NCSX is predicted to be $B_{rnm}/B \approx 6\text{x}10^{-4}$.

Because of the strong plasma flow predicted to be driven in NCSX by the ambipolar electric field, the shielding of resonant perturbations is predicted to be strong, stronger than in neutral beam heated discharges in DIII-D. In particular, the q = 2 flux surface in NCSX is predicted to have reduced vulnerability to field errors relative to that in tokamaks. Tokamaks are most vulnerable to field error penetration just before the neutral beams are turned on, when the flow is diamagnetic. The measured penetration threshold in an ohmic DIII-D plasma with a density of $2\text{x}10^{19}$ m^{-3} is $B_{r21}/B \approx 2\text{x}10^{-4}$.

We compare the predicted penetration threshold with the resonant magnetic field perturbation amplitude produced by the unhealed NCSX coils. For this purpose, we initialize a PIES calculation with a VMEC equilibrium and we run through one iteration of the PIES code. VMEC provides the equilibrium under the constraint that the flux surfaces are preserved, as is appropriate if the flux surfaces have been preserved by shielding due to plasma flow. PIES calculates the resonant magnetic fields produced by the plasma and coil currents. In practice, the PIES diagnostic provides the magnetic island width corresponding to these resonant fields. We back out the value of the resonant field from the equation for the island width in terms of the resonant field: $w^2 = (16/\iota' m)(B_1^r / B_0^\phi)_{nm}$, where the superscripts here represent contravariant components. The m = 5, n = 3 island width for the unhealed coils is determined to be about 18% of the minor radius, corresponding to $B_{nm}^r \approx 15$ G, or $B_{rnm}/B \approx 1.3\text{x}10^{-3}$. This is above the threshold for field error penetration determined above. We conclude that some modification of the coil design to suppress resonant magnetic field components is necessary. The modified coils described in this chapter are expected to be more than adequate for that purpose, and shielding of resonant fields due to the relatively strong ambipolar flow in NCSX is likely to remove the small residual islands for appropriate startup scenarios.

3.10 Conclusions

The initial calculation of the three-dimensional equilibrium is performed with the VMEC code. This code makes the simplifying assumption that nested magnetic flux surfaces exist, which greatly increases the speed of the calculation and thus makes possible the routine assessment of stability and transport for candidate equilibria. To calculate the three-dimensional equilibria with islands and stochastic regions the PIES code is used, which relaxes the assumption of nested flux surfaces at the cost of computational speed. Critical improvements have been made to both VMEC and PIES during the course of the NCSX design.

PIES has been used to improve the flux surface quality of the reference configuration by small modifications that reduce the resonant magnetic field components. In fixed boundary equilibria, the island content is reduced by alteration of the boundary, and in free-boundary equilibria, the island content is reduced by variation of the coil geometry.

The latter technique, termed coil-healing, in essence amounts to a free-boundary stellarator plasma-coil design algorithm, which adjusts the coil geometry to obtain a plasma equlibrium with selected islands suppressed, while simultaneously preserving certain engineering constraints and stability measures. It is this method which derived the healed coil set, M45h, referred to throughout this document.

The flux surface quality of plasma configurations generated by the healed coil set, M45h, have been extensively studied. Using a multi-filament coil description to model the finite build of the coils, the PIES calculation shows that the flux surface quality is improved relative to that of the single filament healed coils. Vacuum states with various rotational transform profiles are shown which confirm that the healed coils allow good flux surfaces in the vacuum. Also, a comparison of the healed coils with the unhealed coils for an alternative high β configuration from the startup modeling (Chapter 9) shows that the healed coils produce improved flux surface quality, relative to the unhealed coils, for configurations for which the coils were not optimized. Having reduced the amplitude of the resonant magnetic field components produced by the coils in the reference configuration, the flux surfaces are improved in other configurations as well. Additional calculations with PIES, examining five snapshots in a startup scenario, are described in Chapter 9.

Finally, neoclassical, $\chi_\perp / \chi_{//}$, and flow effects are estimated. Neoclassical effects are predicted to produce a substantial reduction in the island widths relative to those calculated by the PIES code. The effect of finite $\chi_\perp / \chi_{//}$ is to give a threshold island width, $w_0 \approx 0.035$ a, below which islands have little impact on confinement. The strong ambipolar plasma flow that is calculated for NCSX is predicted to shield out resonant magnetic fields at the rational surfaces, reducing the sensitivity to field errors and removing many of the islands that appear in the PIES calculations.

Including the corrections due to the finite neoclassical and $\chi_\perp / \chi_{//}$ effects, an assessment of the flux surfaces as calculated by PIES for a range of configurations, including the reference configuration with single and multi-filament coils, five different vacuum configurations, and five equilibria representing snapshots at different times in a startup scenario (Chapter 9), indicate that the flux surfaces for the healed coil set, M45h, are acceptable.

References

[1] HIRSHMAN, S.P., Lee, D.K., Comput. Phys. Comm. **39** (1986) 143.
[2] HIRSHMAN, S.P., Van Rij, W.I. and MERKEL, P., Comp. Phys. Commun. **43** (1986) 143.
[3] KESSEL, C. E. Nuc. Fus., **34**, (1994) 1221.
[4] HIRSHMAN, S. Phys. Fluids, **31**, (1988) 3150.

[5] HARRIS, G. R. EUR-CEA-FC-1436, (1991).
[6] WHITE, R. B. AND CHANCE, M. S. Phys. Fluids **27**, (1984) 2455.
[7] WHITE, R. B. Phys. Fluids B **2**, (1990) 845.
[8] SPONG, D. http://www.pppl.gov/ncsx/Meetings/Physics_Mtgs/1999/June/june.html.
[9] REIMAN, A., and Greenside, H. S., Comput. Phys. Commun. **43** (1986) 157.
[10] REIMAN, A., and Greenside, H. S., J. Comput. Phys. **75** (1988) 423.
[11] GREENSIDE, H., REIMAN, A., and SALAS, A., J. Comput. Phys. **81** (1989) 102.
[12] Reiman, A. and Pomphrey, N. J. Comput. Phys. **941** (1991) 225.
[13] MONTICELLO, D. A., MERKEL, P., JOHNSON, J. L., and REIMAN, A. H., Proceedings of Tenth International Conference on Stellarators, Madrid (1995).
[14] DELUCIA, J., JARDIN, S. C., and TODD, A. M. M., J. Comput. Phys. **37** (1980) 183.
[15] CHODURA, R. and SCHLUTER, A., J. Comput. Phys. **41** (1981) 68.
[16] JOHNSON, J. L., MONTICELLO, D. A., REIMAN, A. H., et al., Comp. Phys. Commun. **77** (1993) 1.
[18] MERKEL, P., JOHNSON, J. L., MONTICELLO, D. A., et al., Proceedings of the Fourteenth International Conference on Plasma Physics and Controlled Nuclear Fusion Research paper IAEA-CN-60 | D-P-II-10 (1994).
[19] REIMAN, A. H. and GREENSIDE, H. S., J. Comput. Phys. **87** (1990) 349.
[20] JOHNSON, J. L., MONTICELLO, D. A., and REIMAN, A. H., Proceedings of the 15th International Conference on the Numerical Simulations of Plasmas (1994).
[21] A. H. Reiman and H. S. Greenside, J. Comput. Phys. **87** (1990) 349.
[22] A. H. Reiman and D. Monticello, Phys Fluids B **3** (August 1991) 2230.
[23] A. H. Reiman and D. Monticello, Nucl. Fusion **32** (1992) 1341.
[24] R. J. Goldston, et al Fusion Technol. **21** (May 1992) 1039.
[25] A. Lopez Fraguas, A. Salas, A. H. Reiman, D. A. Monticello, and J. L. Johnson, in Proceedings of the Ninth Kiev International Conference on Plasma Theory, July, 1992, p. I-577.
[26] S. C. Jardin, et al in Proceedings of the Fourteenth International Conference on Plasma Physics and Controlled Nuclear Fusion Research, (Wurzburg, Germany, September 1992) (International Atomic Energy Agency, Vienna, Austria), Paper IAEA-CN-56/D-4-13.
[27] D. A. Monticello, A. H. Reiman, and C. Y. Wang, in Proceedings of the Ninth International Workshop on Stellarators, (International Atomic Energy Agency, Vienna, Austria, 1993), p. 114.
[28] A. Salas, A. Lopez Fraguas, A. H. Reiman, D. A. Monticello, and J. L. Johnson, in Proceedings of the Ninth International Workshop on Stellarators, (International Atomic Energy Agency, Vienna, Austria, 1993) p.127.
[29] P. Merkel, J. L. Johnson, D. A. Monticello, and A. H. Reiman, in Proceedings of the Ninth International Workshop on Stellarators, (International Atomic Energy Agency, Vienna, Austria, 1993), p. 133.
[30] J. L. Johnson, D. A. Monticello, A. H. Reiman, and C. Wang, in Proceedings of the Ninth International Workshop on Stellarators, (International Atomic Energy Agency, Vienna, Austria, 1993), p. 121.
[31] J. L. Johnson, D. A. Monticello, A. H. Reiman, A. Salas, A. L. Fraguas and S. P. Hirshman, Comp. Phys. Commun. **77** (September 1993) 1.
[32] J. A. Schmidt, et al, J. Fus. Energy **12** (1993) 221.

[33] J Nuhrenberg, et al, Plasma Physics and Controlled Fusion, **35** Supplement (December 1993) B115.
[34] J. Manickam, et al, Phys. Plasmas **1** (1994) 1601.
[35] P. Merkel, J. L. Johnson, D. A. Monticello, A. H. Reiman, A. Salas, and A. L. Fraguas, Proceedings of the Fifteenth International Conference on Plasma Physics and Controlled Nuclear Fusion Research, (International Atomic Energy Agency, Vienna, Austria, September 1994).
[36] D. A. Monticello, J. L. Johnson, A.H.Reiman, and P.Merkel, in Proceedings of the Tenth International Workshop on Stellarators, EUR-CIEMAT **30** (1995) p. 45.
[37] R. J. LaHaye et al, in Proceedings of the Sixteenth IAEA Fusion Energy Conference, (International Atomic Energy Agency, Vienna, Austria, 1996) Paper F1-CN-64/AP1-21.
[38] A. Reiman, L.P. Ku, D. Monticello, C. Nuehrenberg, and W. Cooper, Plasma Physics Reports **23** (1997) 472.
[39] S. Arndt, P. Merkel, D. A. Monticello and A. H. Reiman, Phys. Plasmas **6** (1999) 1246.
[40] A. Reiman, et al, Phys. Plasmas **8** (2001).
[41] H. Gardner and B. Blackwell, Nucl. Fusion **33** (1993).
[42] C. C. Hegna and J. D. Callen, Phys. Plasmas **1** (1994) 3135.
[43] S.R. Hudson and R.L. Dewar. Analysis of perturbed magnetic fields via construction of nearby integrable field. *Phys.Plasmas,* **6(5)** (1999) 1532.
[44] A.J. Lichtenberg and M.A. Lieberman. *Regular and Chaotic Dynamics, 2nd ed.* Springer-Verlag, New York, 1992.
[45] J.D. Meiss. Symplectic maps, variational principles & transport. *Reviews of Modern Physics*, **64(3)** (1992) 362.
[46] W. H. Press, B. P. Flannery, S. A. Teukolsky, and W. T. Vetterling. *Numerical Recipes in Fortran 77 : The art of scientific computing*. Cambridge University Press, Cambridge, U.K.
[46a] R.L.Dewar and S.R.Hudson and P.Price., Physics Letters A, 194:49, 1994
[47] C. C. Hegna and J. D. Callen, Phys. Plasmas **1** (1994) 3135.
[47a] K. Narihara et al, Phys. Rev. Lett **87**, 135002-1 (2001).
[47b] N. Ohyabu et al, Phys. Rev. Lett **88**, 055005-1 (2002).
[48] P. H. Rutherford, Phys. Fluids **16** (1973) 1903.
[49] J. D. Callen, et al., in "Plasma Physics and Controlled Nuclear Fusion Research", Kyoto (IAEA, Vienna, 1987). **2**, p. 157.
[50] C. C. Hegna, et al., Plasma Phys. Controlled Fusion **35** (1993) 987.
[51] R. Fitzpatrick, Phys. Plasmas **2** (1995) 825.
[52] Z. Chang, et al., Phys. Rev. Lett. **74** (1995) 4663.
[53] D. R. Mikkelson, NCSX Project Meeting (January, 2001); see also Section 7.
[54] F. L. Hinton and M. N. Rosenbluth, Phys. Fluids **16** (1973) 836.
[55] R. J. Goldston, private communication (June, 2000).
[56] R. Fitzpatrick and T.C. Hender, Phys. Fluids B **3**, 644 (1991).
[57] T. C. Hender et al, Nucl. Fusion **32**, 2091 (1992).
[58] R. J. LaHaye et al, Phys. Fluids B **4**, 2098 (1992).
[59] R. J. LaHaye et al, Nucl. Fusion **32**, 2119 (1992).
[60] R. J. Buttery et al, Nucl. Fusion **39**, 1827 (1999).
[61] R. Fitzpatrick, Phys. Plasmas **5**, 3325 (1998).